TECHNISCHE
UNIVERSITÄT
WIEN
Vienna University of Technology

INSTITUT FÜR
MECHANIK UND
MECHATRONIK
Mechanics & Mechatronics

DIPLOMARBEIT

Dynamic modeling and control of a fluidized bed methanation reactor

ausgeführt zum Zwecke der Erlangung des akademischen Grades eines Diplom-Ingenieurs
unter der Leitung von

Univ.Prof. Dr. Martin Kozek
Institut für Mechanik und Mechatronik
Abteilung für Regelungstechnik und Prozessautomatisierung

eingereicht an der Technischen Universität Wien

Fakultät für Maschinenwesen und Betriebswissenschaften

von

Grossgasteiger Leander
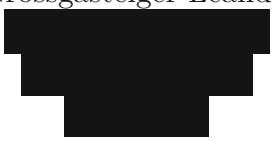

Wien, am 31. August 2022

Grossgasteiger Leander

Eidesstattliche Erklärung

Ich erkläre eidesstattlich, dass ich die Arbeit selbständig angefertigt, keine anderen als die angegebenen Hilfsmittel benutzt und alle aus ungedruckten Quellen, gedruckter Literatur oder aus dem Internet im Wortlaut oder im wesentlichen Inhalt übernommenen Formulierungen und Konzepte gemäß den Richtlinien wissenschaftlicher Arbeiten zitiert, durch Fußnoten gekennzeichnet bzw. mit genauer Quellenangabe kenntlich gemacht habe.

Wien, am 31. August 2022 Grossgasteiger Leander

Danksagung

An diese Stelle möchte ich mich noch bei den Personen bedanken, welche es mir möglich machten, diese Arbeit und mein Studium abzuschließen.

Allen voran möchte ich meinen Betreuern Stanger Lukas und Alexander Bartik danken. Sie nahmen sich immer Zeit, wenn ich ihre Hilfe benötigte und konnten halfen mir mit guten Ideen und Ratschlägen weiter. Vielen Dank euch Zweien!

Ein besonderes Dankeschön möchte ich auch an Professor Kozek Martin ausrichten. Seine Tür stand mir immer offen, um besondere Fragestellungen und Probleme zu diskutieren. Vielen Dank!

Des Weiteren möchte ich mich auch herzlich bei meinen Eltern bedanken. Ihre Unterstützung machte mir diese Ausbildung erst möglich. Danke euch für die Geduld und Fürsorge die ich von euch geschenkt bekommen habe, ich weiß das sehr zu schätzen.

Zu guter Letzt möchte ich mich auch bei meinen Freunden und Studienkollegen bedanken, welche mich durch diese schöne Zeit begleitet haben. Ganz besonders danke ich hier Mayr Theresa, die mich immer unterstützt hat und mich motiviert hat, wenn es mal nicht so gut lief. Vielen Dank!

Kurzfassung

Die Produktion von synthetischem Erdgas (SNG) aus biogenen Rohstoffen kann dazu beitragen, die Treibhausgasemissionen zu reduzieren und mehr Unabhängigkeit von Erdgasimporten zu erlangen. Ein Teilprozess bei der SNG Erzeugung ist die Methanierung, bei der Produktgas zu Roh-SNG umgewandelt wird. In dieser Arbeit wird eine Methode zur dynamischen Modellbildung einer Methanierung im Wirbelschichtreaktor vorgezeigt. Unter Verwendung bestehender Modelle aus der Literatur und Anpassung ihrer Parameter durch experimentelle Daten wird ein Modell geschätzt, welches das nichtlineare, dynamische Verhalten des Wirbelschichtreaktors der TU Wien beschreibt. Das Modell wird durch Untersuchungen am Wirbelschichtreaktor validiert. Zur Optimierung des Methanierungsprozesses wird ein Temperaturregler vorgestellt, um den Methangehalt im Roh-SNG zu maximieren. Die Kombination eines PI-Reglers mit einer stationären Vorsteuerung ergibt eine effiziente Reglerstruktur. Schlussendlich wird die Leistungsfähigkeit und die Robustheit des Reglers anhand von Simulationen mit einem Anlagenmodell mit veränderten Modellparametern gezeigt.

Abstract

Synthetic natural gas (SNG) production from biogenic resources can help reduce greenhouse gas emissions and decrease the dependency from natural gas imports. A subprocess of SNG production is the methanation, where raw-SNG is produced from product gas. In this work, a method that enables the dynamic modeling of the fluidized bed methanation reactor is presented. Using existing models from literature, fitting their parameters to the process and considering experimental data, a model that describes the non-linear, dynamic behavior of the fluidized bed reactor of TU Wien is estimated. The model is validated by investigations in the fluidized bed reactor. To optimize the methanation process, a temperature controller is presented to maximize the methane content in the raw-SNG. An efficient controller is designed by combining a stationary feed-forward controller and a PI controller. Finally, the performance and robustness of the controller is shown by simulations using a plant model with changes in the model parameters.

Contents

Chapter 1

Introduction

Today, natural gas is a widely utilized energy source for heating and production of electrical energy. Figure 1.1 shows that natural gas is highly used in the industrial, residential and service sectors. Despite its popularity as an energy carrier, the obvious downside of natural gas is that it is a non-renewable and finite resource. An additional problem is the CO_2 released during the combustion of natural gas. CO_2 is a greenhouse gas and contributes to global warming.

Biomass-to-Gas (BtG) processes include all processes that produce gases out of renewable organic feedstock. That is why they are considered an alternative to gas production from fossil sources. A much-studied BtG-Process is synthetic natural gas (SNG) production.
With the development of the SNG process, the downsides of natural gas can be addressed. Firstly, natural gas can be synthesized out of carbonaceous feedstock, which solves the finiteness of the resource. Secondly, by using renewable organic feedstock to produce SNG, only CO_2, which was previously bound from the atmosphere, gets released during the process and later during the combustion of SNG.

Methanation is an important sub-process of the SNG process chain. During methanation, the product gas from gasification is converted into raw-SNG. Taking thermodynamics and kinetics of the reaction into account, an optimal temperature is given where the CH_4 output can be maximized. Optimizing the methanation leads to an improvement of the whole SNG process.

In this work, a dynamic model of a fluidized bed methanation reactor is developed. After a brief overview of SNG processes and a detailed view of the methanation, the dynamic model of the fluidized bed methanation and a thermal model that describes the temperature development in the air-cooled reactor over time is presented. Both

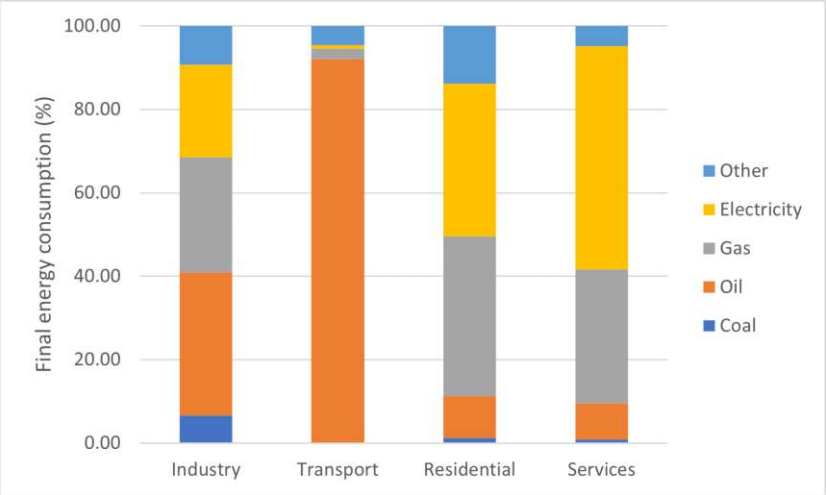

Figure 1.1: Final energy consumption of OECD-countries by sector and source, 2019 [1].

models are validated with data from a pilot plant located at TU Wien. A controller, which changes the cooling system's airflow to maintain an optimal reactor temperature, is designed. The controller performance is then tested in simulations.

1.1 Research questions

In this thesis, the following research questions are covered:

What is an appropriate method to dynamically model the conversion of product gas to raw-SNG inside a a fluidized bed methanation reactor and the corresponding cooling system?

What would be an effective controller design to control the temperature of the fluidized bed methanation reactor, taking into account measurable disturbances?

Chapter 2

Theoretical background

This chapter gives an overview of SNG processes. It contains information about the history and the structure of SNG processes. The methanation sub-process is explained in further detail in this chapter, too.

2.1 History and development of the SNG process

The first interest in SNG was aroused in the 1970s in the United States. The increasing demand for natural gas around that time and the oil crisis in the 1970s were the main factors for the development of SNG processes. The first processes, that were developed used coal as feedstock. The high availability of cheap domestic coal made the process feasible and led to the erection of the Great Plains Synfuels Plant by the Dakota Gasification Company. It was the first commercial plant built and was able to produce 4.8 million m^3 SNG per day [12, 13].

In the early 2000s, the research around SNG processes in America and Europe experienced another upswing, due to rising natural gas prices and the wish for less dependency on natural gas imports. It was also at that time, that early attempts were made to use biomass as a renewable organic feedstock for SNG production to reduce greenhouse gas emissions. Besides different pilot plants, even a commercial plant that used biomass to produce SNG was erected in Gothenburg. [3, 12].

2.2 SNG process chain

The process chain for biomass conversion to SNG can be divided into four sub-processes: gasification, gas cleaning, methanation and gas upgrading. Figure 2.1 shows a basic

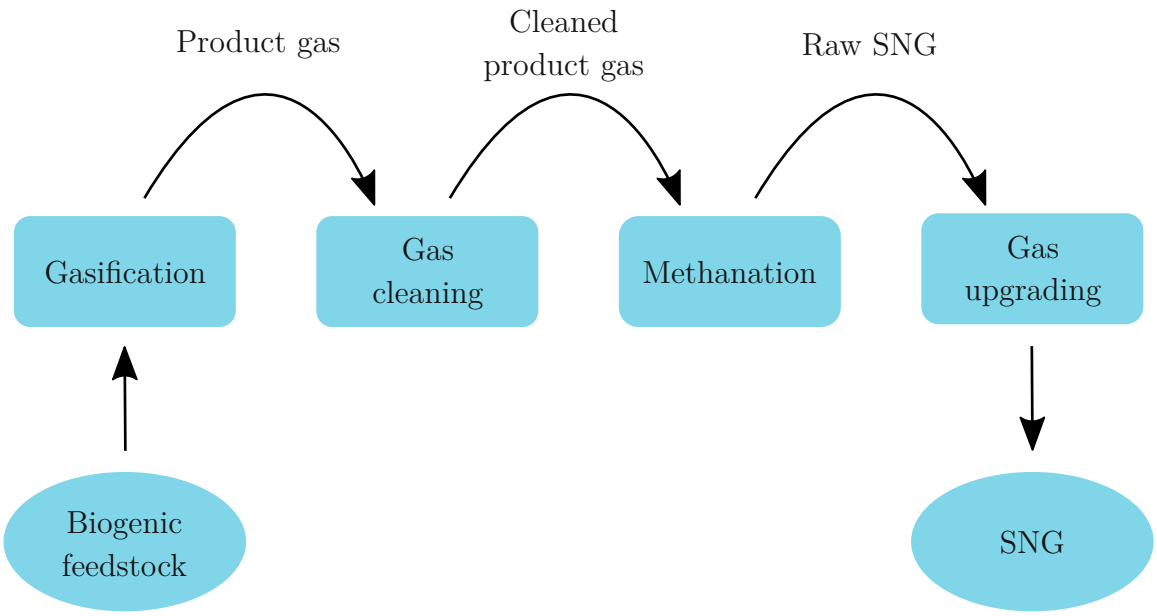

Figure 2.1: Basic flowsheet of a SNG process, divided into sub-processes and their respective intermediates.

flowsheet of the four sub-processes and their respective intermediates. The differences between various SNG processes lie mostly in the design of the four sub-processes [14].

2.2.1 Gasification

This thermochemical process describes the conversion of solid carbonaceous feedstock into product gas with the help of a gasification agent. During the process, the biomass particles undergo a conversion that can be divided into three main conversion steps: drying, devolatilization and gasification. Figure 2.2 shows a brief overview of these conversion steps demonstrated by the example of a biomass particle. As a result, a solid ash fraction and product gas are obtained. Product gas contains mostly CO, H_2, CO_2 and CH_4. However, the composition of product gas depends strongly on which gasification agent is used. For example, if air (21% O_2, 79% N_2) is used for gasification, high amounts of nitrogen will be found in the product gas. The usage of steam as gasification agent results in higher amounts of hydrogen, whereas pure oxygen increases the number of carbon oxides (CO,CO_2)[2, 15, 16]. Technically relevant gasification agents are O_2, H_2O, CO_2 and H_2. The gasification agent is also connected to the type of heat input into the system. As the gasification process is an overall endothermic process, heat has to be provided. It can be distinguished between autothermal gasification, if air

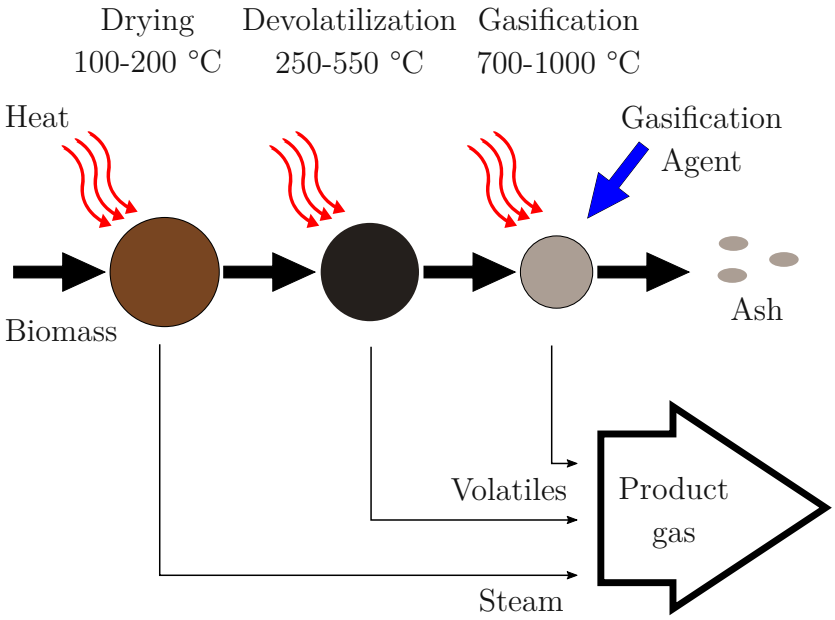

Figure 2.2: Gasification steps from biomass to product gas [2]

or a O_2/H_2O-mixture are the gasification agent and allothermal gasification, when H_2O or CO_2 are used as gasification agent. For autothermal gasification, heat is provided by partial combustion of the feedstock. On contrary, allothermal gasification relies on an indirect heat source [2].

Dual fluidized bed gasification (DFB)

Figure 2.3 shows a schematic diagram of the DFB gasification process. The DFB is divided into two sections: a gasification reactor and a combustion reactor. The gasification reactor is a bubbling fluidized bed reactor and the combustion reactor is a fast fluidized bed reactor. Both reactors are connected with each other. That makes the circulation of bed material possible, which is essential for this application. Biogenic feedstock is gasified with steam in the gasification reactor, resulting in product gas and a char fraction. The remaining char is transported to the combustion reactor, together with the circulating bed material. There, the char is combusted with air. The heat released during the combustion heats up the bed material and serves as the heat source for gasification. The DFB gasification is therefore allotherm. Due to the separation of the flue gas and the product gas stream, the product gas is nitrogen-free [17, 3].

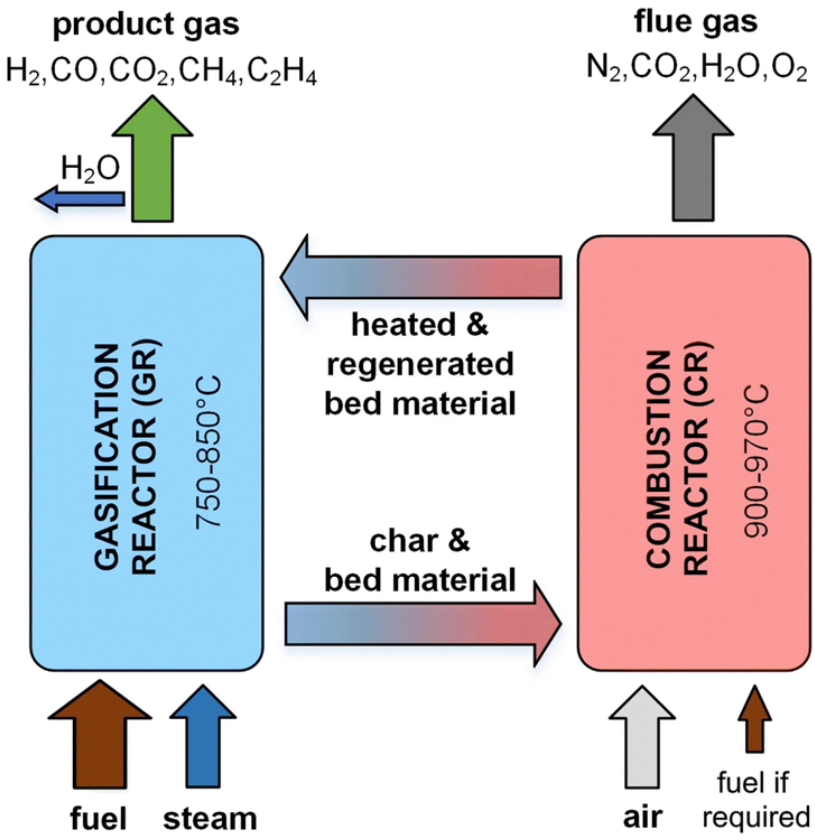

Figure 2.3: Basic principle of a dual fluidized bed gasification process [3].

2.2.2 Gas cleaning

Product gas from the gasification contains, besides the main components, also some unwanted impurities. These contaminants mainly include tars, particulate matters, H_2S, NH_3 and HCl. If not removed, these impurities enter the methanation reactor where they cause catalyst deactivation and poisoning. Additionally, the product gas cleaning prevents downstream applications from clogging or corrosion. More information about gas cleaning can be found in [18, 19].

2.2.3 Methanation

Methanation is the sub-process around which this work revolves. Because of that, this section gives a more detailed overview of the methanation sub-process.

Fundamentals

The primary aim of methanation processes is the conversion of hydrogen and carbon oxides into methane-rich gas. Today, the process is mainly used to produce raw-SNG out of product gas as well as eliminate trace CO contents in hydrogen-rich gases for example during the ammonia synthesis [20]. The main reaction that occurs during the process is the CO methanation reaction (2.1), which was discovered by Sabatier and Senderens in 1902 [21].

$$\mathrm{CO} + 3\,\mathrm{H_2} \rightleftharpoons \mathrm{CH_4} + \mathrm{H_2O} \qquad \Delta H_R^{298\mathrm{K}} = -205.9\frac{\mathrm{kJ}}{\mathrm{mol}} \tag{2.1}$$

The reaction is fast and highly exothermic. Typical product gases from gasification can not reach the required H_2/CO ratio of 3, which is the stoichiometric composition required according to (2.1). Therefore, the H_2/CO ratio can be adjusted by the water-gas shift reaction (2.2) [22].

$$\mathrm{CO} + \mathrm{H_2O} \rightleftharpoons \mathrm{CO_2} + \mathrm{H_2} \qquad \Delta H_R^{298\mathrm{K}} = -41.1\frac{\mathrm{kJ}}{\mathrm{mol}} \tag{2.2}$$

The earliest recording of this reaction dates back to 1888. It is a moderately exothermic reaction and thermodynamically favored at low temperatures [23]. Especially for low H_2/CO ratios, the water-gas shift reaction converts some of the carbon monoxide in the presence of water into additional hydrogen. The downside is the simultaneous production of carbon dioxide, which reduces the raw-SNG quality. However, it is also possible to produce methane out of carbon dioxide and hydrogen.

$$\mathrm{CO_2} + 4\,\mathrm{H_2} \rightleftharpoons \mathrm{CH_4} + 2\,\mathrm{H_2O} \qquad \Delta H_R^{298\mathrm{K}} = -164.8\frac{\mathrm{kJ}}{\mathrm{mol}} \tag{2.3}$$

The so called CO_2 methanation (2.3) is a linear combination of (2.1) and (2.2). CO gets adsorbed much faster on the catalyst than CO_2. Because of that, the CO_2 methanation is strongly inhibited as long as there is enough CO present to cover the catalyst sites [20].

Besides the main species, the product gas can also contain higher hydrocarbons. Equation (2.4) shows the hydrogenation of higher hydrocarbons by the example of ethylene [24].

$$C_2H_4 + 2\,H_2 \longrightarrow 2\,CH_4 \qquad \Delta H_R^{298K} = -201.7\frac{kJ}{mol} \tag{2.4}$$

In addition, it is characteristic of the methanation process that a significant volume contraction takes place throughout the reactor. Based on the mole number change in (2.1) it becomes apparent, that the volume contraction can be up to 50% [9].

Catalysts

Thermodynamically, the methanation process is favored at low temperatures. Therefore, it is necessary to use catalysts to optimize the kinetic behavior. The selection of the catalyst for the heterogeneously catalyzed methanation reactions is of great importance. Many metals, especially from groups 8-10 in the periodic table are active towards the methanation reaction [4]. Their specific activities and their selectivity were ranked by Vannice et al. [25]:

- Activity: Ru>Fe>Ni>Co>Rh>Pd>Pt>Ir
- Selectivity: Pd>Pt>Ir>Ni>Rh>Co>Fe>Ru

Besides a good selectivity and activity, the ideal catalyst should also be stable at high temperatures to prevent sintering and it should have high activities at low temperatures where the methanation reaction is favored [26]. Because of its high performance-to-cost ratio nickel is one of the most studied active materials for methanation [26].
Not only the actives metals but also the support materials and promoters are widely studied. As support materials, Al_2O_3, TiO_2 and SiO_2 are common, whereas promoters are likely to be small amounts of cobalt, molybdenum, magnesium or tungsten [22, 26].

Methanation reactors

As stated in the reviews of Rönsch [4] and Seemann [22], methanation reactors can be divided into three groups, namely adiabatic fixed-bed reactors, isothermal reactors and polytropic reactors. A classification can be made based on the Semenov number (2.5).

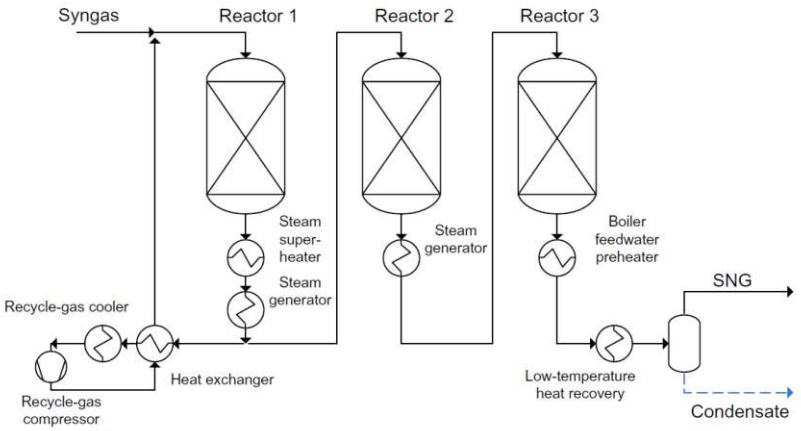

Figure 2.4: TREMP process with three adiabatic fixed-bed reactors, intermediate cooling and gas recirculation [4].

$$Se = \frac{heat\ production\ rate}{cooling\ rate} \tag{2.5}$$

While it goes towards infinity for adiabatic reactors, the Seminov number of an isothermal reactor is close to zero. Everything in between are polytropic reactors [27].

Adiabatic fixed-bed reactors ($Se \to \infty$) This reactor concept is well developed and used in commercial processes like the Lurgi Coal-to-SNG process [28] or the Haldor Topsoe TREMP process [29]. Adiabatic fixed-bed reactors have been used for years as the final purification steps in ammonia plants to get rid of carbon oxides. In such plants, the reactor operates at nearly isothermal conditions, since the reactants are highly diluted [22, 29]. However, given the high amounts of carbon monoxide and hydrogen during the SNG process, the above-mentioned reactors have problems with heat transfer. The high heat of reaction of the methanation reaction has to be dissipated to keep the reactor temperature at reasonable values. Too high reactor temperatures lead to carbon formation or sintering of the catalyst and thus to deactivation of the latter [29, 30]. In addition, methanation is an exothermic reaction and occurs preferentially at low temperatures.

To oppose this problem, commonly used adiabatic fixed-bed applications for methanation processes are divided into a cascade of three or more reactors with intermediate cooling between them. Furthermore, there is often a recirculation step of the gas between the first and the second reactor, which is used to decrease the temperature in both of them [28, 29]. An example of a methanation process,

that uses adiabatic fixed-bed reactors is given in Figure 2.4.

The main advantages of adiabatic fixed-bed reactors are the high reaction rate and the possibility to produce steam at high temperatures [4].

Polytropic reactors ($0 < Se < \infty$) In general, polytropic reactors are a combination between adiabatic and isothermal reactors. On one side, an attempt is made to retain the high reaction rates of adiabatic fixed-bed reactors while on the other side the research tends to higher cooling rates and heat transfer, which lowers the temperature of hot spots in the reactor. The latter favors higher conversion rates and protects the catalysts from deactivation [31, 4, 32]. Reactor types that can be described as polytropic are cooled fixed-bed reactors and structured reactors. Cooled fixed-bed reactors use different cooling approaches to reduce hot-spot formation without diluting the feed gas stream. Reactors developed by Linde and Etogas GmbH can be named in this context [31, 33]. On the contrary, structured reactors attempt to increase the heat and mass transfer with improved structures like microchannels or honeycomb structures [4]. In this field, the application of 3-D printing is very promising, because it enables a feasible fabrication of complex and geometrically customized catalytic designs [34].

Both of the polytropic reactor concepts lead to higher conversion rates since the outlet temperature is reduced in comparison to adiabatic fixed-bed reactors. However, these developments have not yet reached a commercial level [22].

Isothermal reactors ($Se \to 0$) Isothermal reactors are characterized by a high heat transfer, which allows an operation at a nearly constant temperature throughout the reactor. Two reactor types fulfill these conditions, namely fluidized-bed reactors and three-phase reactors [4].

Figure 2.5 shows the basic principle of a three-phase reactor. Three-phase reactors are slurry reactors, where fine catalyst particles are suspended in a liquid phase. Simultaneously, product gas is added via a gas distributor. These reactors can be operated isothermally because the heat of reaction can be dissipated into the liquid phase. Three-phase reactors are less prone to quick temperature changes, due to the high heat capacity of the liquid phase. That makes it easier to control the temperature accurately and effectively. Possible drawbacks include evaporation or decomposition of the heat transfer liquid, as well as additional mass transfer limitations due to the liquid phase [35, 5].

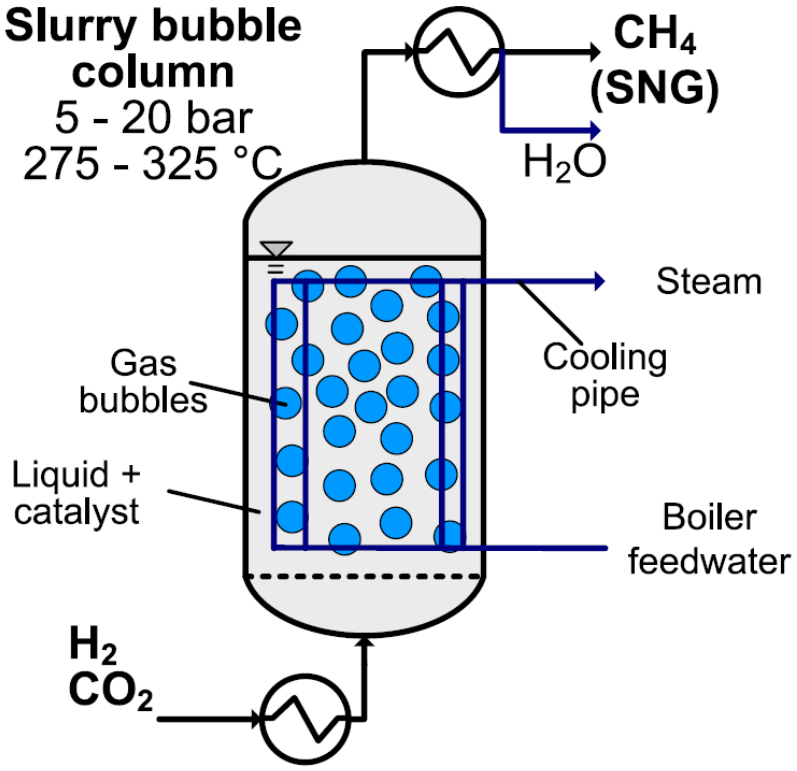

Figure 2.5: The slurry-bubble-column reactor as example for a three-phase reactor [5].

Fluidized-bed reactors are commonly used for many industrially important solid catalyzed gas-phase reactions. Due to constant particle movement during processes, the mass and heat transfer in fluidized-bed reactors are excellent. Because of that, there are no hot spots throughout these nearly isothermal reactors [36, 7]. Good heat and mass transfer during methanation lead to high conversion rates at relatively low temperatures, which favors a higher methane yield. Besides that, the coke formation on the catalyst surface is minimized due to the colliding particles [37]. However, the attrition and entrainment of catalyst particles is a major drawback of this technology [31]. Some examples of fluidized-bed reactors for methanation purposes are given by Kopyscinski [12].

2.2.4 Gas upgrading

The last step of a biomass-to-gas process is the upgrading of raw-SNG. SNG should be able to replace conventional gas in all applications. Therefore, it must meet certain requirements. For raw-SNG, this usually means reducing the proportion of carbon dioxide and water. Depending on the process layout, also a reduction of hydrogen must be considered [38]. The requirements for SNG in Austria can be retrieved from the ÖVGW guideline GB210 [11]. This guideline takes not only the European standards [39, 40] into account, but refers also to elements of the previous ÖVGW guideline. Table 2.1 sums up the requirements that are given by the GB210 guideline.

Water removal can be achieved by condensation, adsorption, absorption or a combination of those methods. Similar to water, carbon dioxide can also be removed by physical or chemical absorption, but there are also other possibilities like pressure swing adsorption, membrane separation or low-temperature separation. Finally, hydrogen removal can be accomplished by pressure swing adsorption or membrane separation [41].

Table 2.1: Requirements for natural gas in Austria [11]

Parameter	Unit	Limits	
		Min.	Max.
Relative density	-	0.555	0.7
Total sulfur content	mg/m^3	n.a.	20
Hydrogen sulfide and carbonyl sulfide	mg/m^3	n.a.	5
Mercaptans	mg/m^3	n.a.	6
Oxygen	mol %	n.a.	0.001
Carbon dioxide	mol %	n.a.	2.5
Hydrocarbon dew point	°C	n.a.	-2
Water dew point	°C	n.a.	-8
Carbon monoxide	mol %	n.a.	0.1
Ammonia	mg/m^3	n.a.	10
Amine	mg/m^3	n.a.	10
Methane number	-	n.a.	65
Hydrogen	mol %	n.a.	10
Wobbe index	MJ/m^3	45.25	54
Upper calorific value	MJ/m^3	33.71	45.18
Nitrogen	mol %	n.a.	5

Chapter 3

System modeling

This chapter deals with the dynamic modeling of the internally circulating fluidized bed reactor of TU Wien. The first parts of the chapter provide the reader with the necessary theoretical knowledge. After that, a method to model the conversion from product gas into raw-SNG is shown. The final part is about modeling the air-cooling system of the reactor.

3.1 Internally circulating fluidized bed reactor (ICFB reactor)

The ICFB reactor consists of two separated reaction zones, which are connected by the circulation of the solid material between the two zones. The reactor is divided by an inserted draft tube into a cylindrical fluidized bed inside the draft tube and an annular fluidized bed outside the draft tube. This setup makes it possible to control the gas velocity in each section independently. Figure 3.1 illustrates the ICFB reactor.

The reactor is operated at atmospheric pressure and temperatures around 300-400 °C. The excess heat of reaction, which is released during the methanation, is dissipated via air cooling. Therefore, the draft tube is cooled with an air perfused coil, whereas the annular region is cooled with a cooling jacket on the outside of the reactor. As bed material, an on-campus developed Ni/-Al_2O_3-catalyst is diluted with unimpregnated Al_2O_3. The thinner pipes in Figure 3.1 are intended for temperature and pressure measurement. The reactor parameters used for modeling the ICFB reactor are given in Table 3.1. Further information about the ICFB reactor can be found in [6].

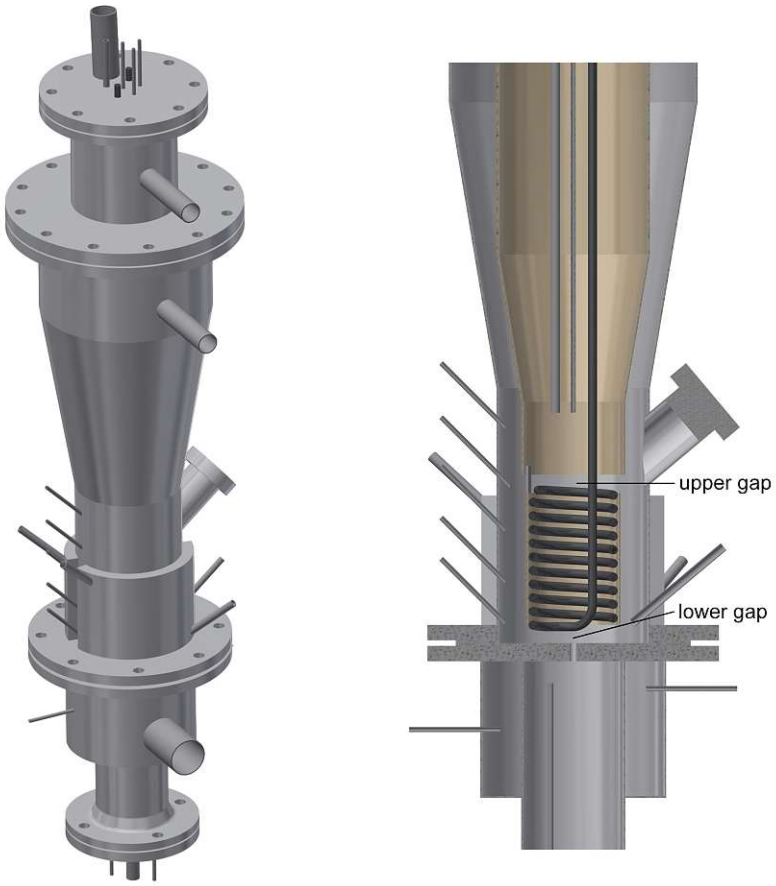

Figure 3.1: Illustration of the ICFB reactor [6].

Table 3.1: Model parameters of the ICFB reactor

Parameter	Abbreviation	Unit	Value
Diameter draft tube	d_{dt}	m	0.07
Inner diameter annular region	$d_{\mathrm{ar,i}}$	m	0.104
Outer diameter annular region	$d_{\mathrm{ar,o}}$	m	0.1643
Height of the catalyst bed	h_{b}	m	0.2
Catalyst mass	m_{cat}	g	1600
Diameter of the catalyst particles	d_{cat}	mm	0.150
Sphericity of the catalyst particles	s_{cat}	-	1
Density of the catalyst particles	ρ_{cat}	kg/m^3	1800

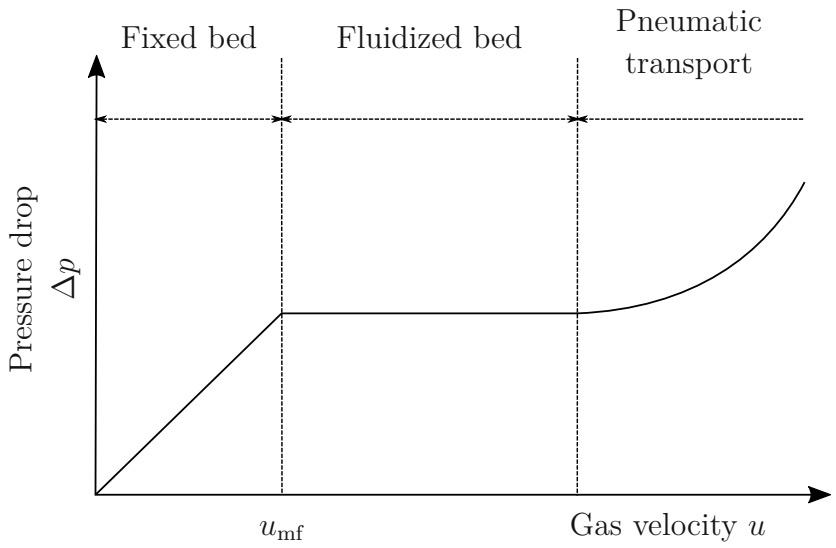

Figure 3.2: Pressure drop/ velocity diagram for fluidized beds [7]

3.2 Fluid dynamics in fluidized beds

The physical behavior of the fluidized bed is described by fluid dynamics. This section introduces different types of fluidized beds and approaches to their modeling are shown. Fluid dynamics do not consider chemical reactions that take place inside the reactor.

3.2.1 Basics

If the combined drag and body forces, exerted by an upward flowing fluid on an assembly of solid particles, exceed the gravitational force that acts on the particles, fluidization of the particulate substance takes place. At this point, the assembly of solid particles behaves like a fluid. The gas velocity at which this effect takes place is called the minimum fluidization velocity (u_{mf}). Figure 3.2 shows the typical behavior of the pressure loss through an assembly of particles with increasing gas velocity. Characteristic for fluidized beds is a constant pressure drop from the moment when u_{mf} is reached [7, 42]. The behavior of fluidized beds depends on the nature of the particles and the gas velocity. Therefore, Geldart [43] classified fluidizable particles into different groups:

Group C: This group includes cohesive powders. Due to the high inter-particle forces of these materials, their fluidization is extremely difficult.

Group A: This group contains materials with small mean particle size and/or a low particle density. Meeting the required fluidization velocity, beds made from these materials expand considerably. By further increasing the gas velocity, the bed

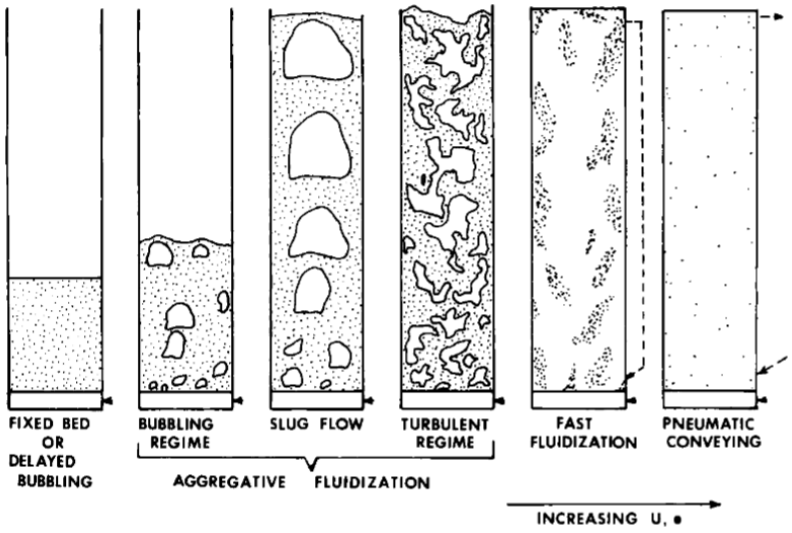

Figure 3.3: Flow patterns in gas-solid fluidized beds for increasing gas velocity [8]

collapses and bubbles begin to form. Those bubbles rise at velocities proportional to their diameter and burst at the bed surface. The bubble rising velocity is higher than the interstitial gas velocity.

Group B: Materials of this group start to form bubbles immediately after the gas velocity reaches u_{mf}. The bed expansion for these materials is negligible. Bubble size increases with bed height and gas velocity. The bubble rising velocity is higher than the interstitial gas velocity. A typical material in this group is coarse sand.

Group D: Large and very dense particles fall into group D. The bubble rising velocity is smaller than the interstitial gas velocity. Additionally, these materials tend to spout.

Figure 3.3 displays the influence of different gas velocities on fluidized beds of Geldart A and B materials. The term *"aggregative fluidization"* describes the non-uniform particle distribution through the bed for the bubbling regime, the slug flow and the turbulent regime. At higher gas velocities, particles are entrained by the gas stream. In this case, recirculation of the entrained particles is necessary to maintain the fluidized bed. Applications with high gas velocities and particle recirculation are called circulating fluidized beds [8, 7].

3.2.2 Fluidized bed models

Aggregative fluidized beds have a non-uniform particle distribution due to bubbles or rising voids that form inside the bed. Therefore, they are usually modeled as multiphase systems. Two-phase and three-phase models are typical approaches [44].

Two-phase model

The two-phase model was first introduced by Toomey and Johnston in 1952. In this model, the fluidized bed consists of two phases: a dense phase and a bubble phase. The dense phase or emulsion phase includes the solid particles and interstitial gas at minimum fluidization velocity. The gas flow that exceeds u_{mf} forms bubbles and is considered in the bubble phase. Both phases are described by separate equations and are connected through inter-phase mass transfer. The disadvantage of the original two-phase theory is its simplification of important physical effects like bubble growth, coalescence and splitting [44, 9].

Three-phase model

Figure 2.5 illustrates the bubbling bed model proposed by Kunii and Levenspiel [45]. In their model, an additional cloud-wake phase is introduced besides the dense and bubbling phase. Based on investigations from Davidson and Harrison, it is assumed, that a thin cloud layer of circulating gas surrounds the rising bubbles in small particle beds (Geldart A). This cloud layer separates the gas inside the bubbles from the gas in the dense phase. Two interchange mass transfer coefficients are necessary to describe the gas interchange between the bubble and dense phase. The size of the cloud layer depends on the particle size. Cloud layers of intermediate particle beds (Geldart B) are large and overlapping and can hardly be distinguished from the emulsion phase. A wake rising behind the bubbles is responsible for the circulation of solid bed material. The bubbling bed model assumes a constant bubble size. Later, Kato and Wen were able to include the bubble growth through the fluidized bed in their bubble assemblage model [46, 9].

3.3 Thermodynamics

The first law of thermodynamics states, that different forms of energy can be converted into each other. Simultaneously, the second law of thermodynamics shows where the limitations of this conversion lie. Because of that, it is possible to calculate the equilibrium output of chemical reactions or reaction systems at given temperatures and

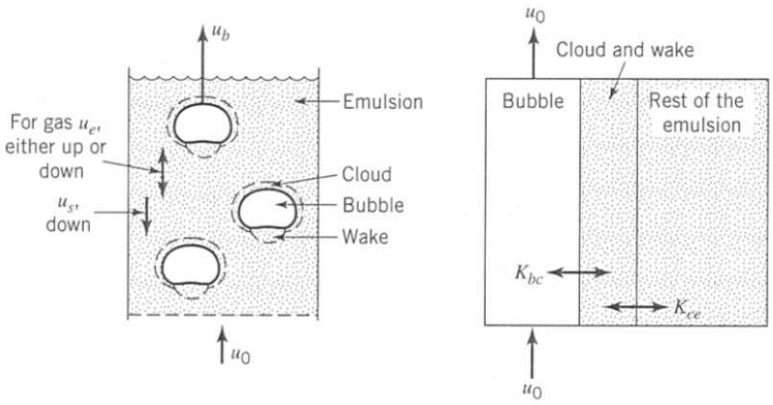

Figure 3.4: Three phase model proposed by Kunii and Levenspiel [9]

pressures [47].

There are various literature sources about the thermodynamics of the methanation reaction system. All sources slightly differ in the number of reactions included in their calculations or investigate the reaction system at different pressures, temperatures as well as the usage of different catalysts [48, 49, 50, 9, 22, 24]. Besides the results that were already mentioned in Section 2.2.3, namely the volume reduction, the highly exothermic behavior of the reaction and the higher conversion rates at low temperatures, thermodynamic investigations led to some additional conclusions.

Firstly, it is obvious that the equilibrium of the methane synthesis (2.1) is pressure-dependent since there is a volume change during the reaction. Higher pressures shift the equilibrium in the direction of smaller volumes, which leads to higher methane and water contents in the raw-SNG. Investigations about water and methane contents in the feed showed that water inhibits CO and CO_2 methanation. Methane in the feed increases carbon formation. On the contrary, carbon formation can be prevented by higher water contents in the feed [48].

Figure 3.5 shows that for both, CO and CO_2 methanation, the equilibrium concentrations shift at approximately 600 °C from products to educts. Figure 3.5b shows additionally, that the water-gas-shift reaction remains active at higher temperatures. Gao et al. [48] investigated also the simultaneous methanation of CO and CO_2. The conversion of both reactants is similar to their respective methanation. They state, that the conversion of CO is always higher than that of CO_2 at temperatures below 600 °C. Furthermore, Gao assumed that no carbon formation takes place, due to the additional

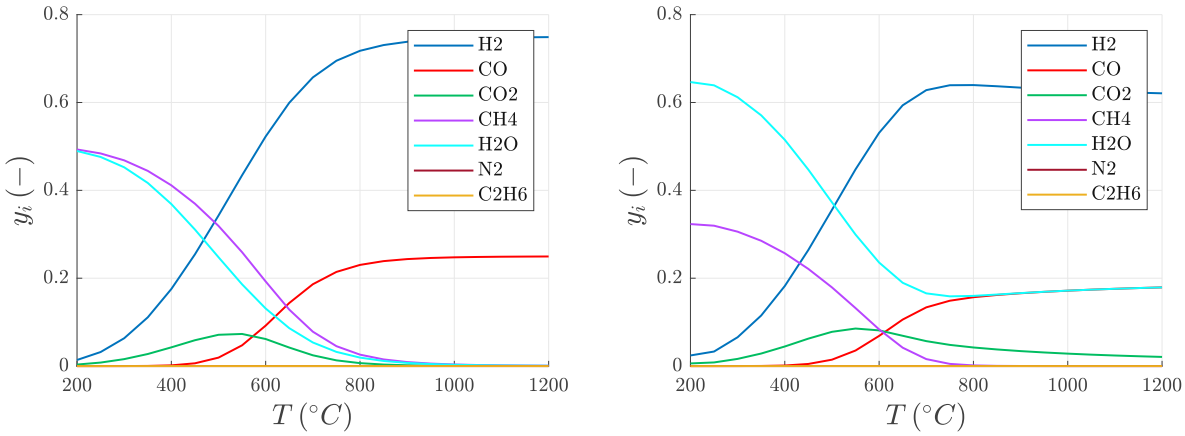

(a) $H_2/CO = 3$ (b) $H_2/CO_2 = 4$

Figure 3.5: Equilibrium concentrations for (a) CO and (b) CO_2 methanation of a stoichiometric gas mixture, at 1 atm and temperatures from 200 to 1150 °C. The water-gas-shift reaction is considered in both figures.

water generated during the CO_2 methanation.

3.4 Kinetics

Although thermodynamic calculations make it possible to estimate the equilibrium state of a reaction system, they are not able to describe the real behavior of reactions. For a better understanding of the actual behavior of reaction systems, kinetics must be taken into account. Arrhenius's law shows the correlation between reaction speed and temperature. The higher the temperature, the higher the reaction speed. Arrhenius's law is given by

$$k = k_0 \cdot e^{-\frac{E_A}{R \cdot T}}, \tag{3.1}$$

where T is the temperature in Kelvin, R is the universal gas constant and k is the rate constant of the reaction. Arrhenius law includes also the activation energy E_A and the pre-exponential factor k_0. The latter can be interpreted as the number of possibilities that a molecule has to react. In theory, k_0 depends on the number of collisions between molecules and the exact orientation of the collisions. The higher the number of collisions with the correct orientation of the colliding molecules, the higher the possibility that a reaction takes place. Because of that, the pre-exponential factor is often tried to

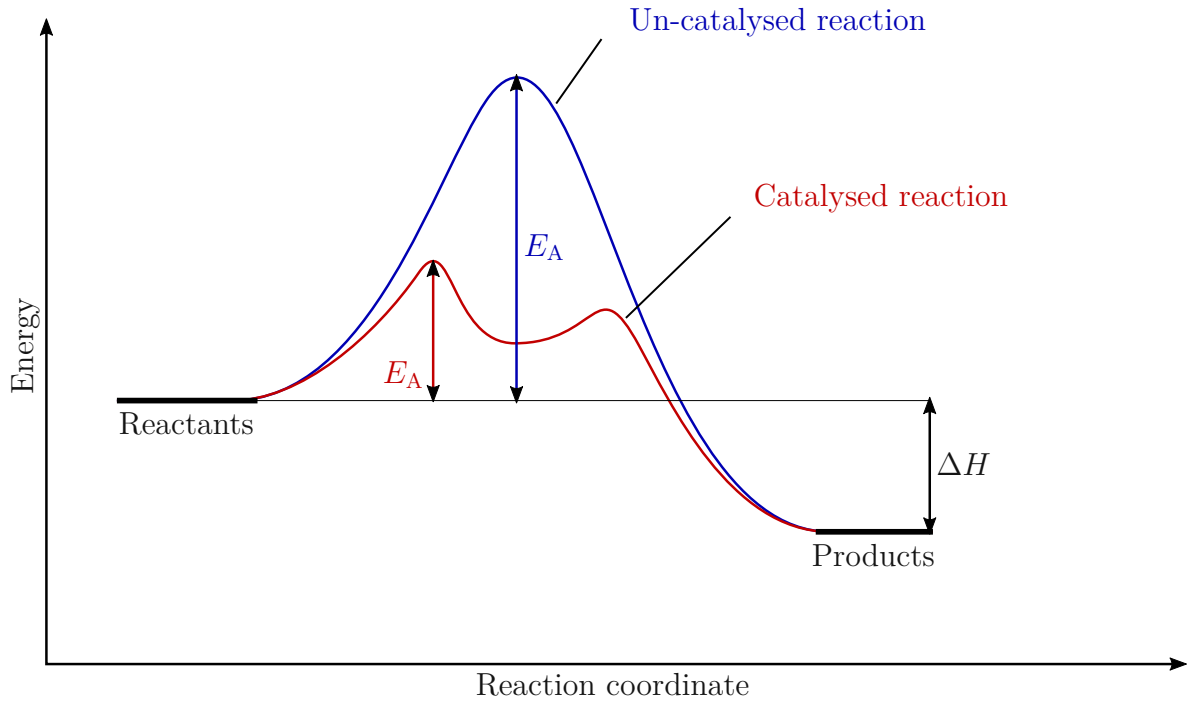

Figure 3.6: Activation energy of catalyzed and uun-catalyzedreactions

be described by the collision theory [51, 52].

Not every collision of two molecules leads to a reaction. Figure 3.6 shows, that reactions need a certain initial energy input before they can take place. Therefore, E_A can be described as the minimal energy that two colliding species must have, for a reaction to occur. Figure 3.6 shows also, that its possible to minimize the activation energy through another reaction path. That alternative reaction path requires one or more intermediate products. This is a typical behavior of catalyzed reactions. For the latter, E_A varies for different types and forms of catalysts. In praxis, k_0 and E_A are often determined from experimental data [51, 52].

3.4.1 First-order reaction approach

To reduce the complexity of their calculations, Cobb and Streeter [53] used a simple first-order rate equation to describe the CO conversion of the methanation reaction for different nickel catalysts. Generally a first-order reaction is described by A $\longrightarrow$ Products [52]. Let C_{CO} be the CO concentration. The change in CO concentration over time r_{CO} is given by

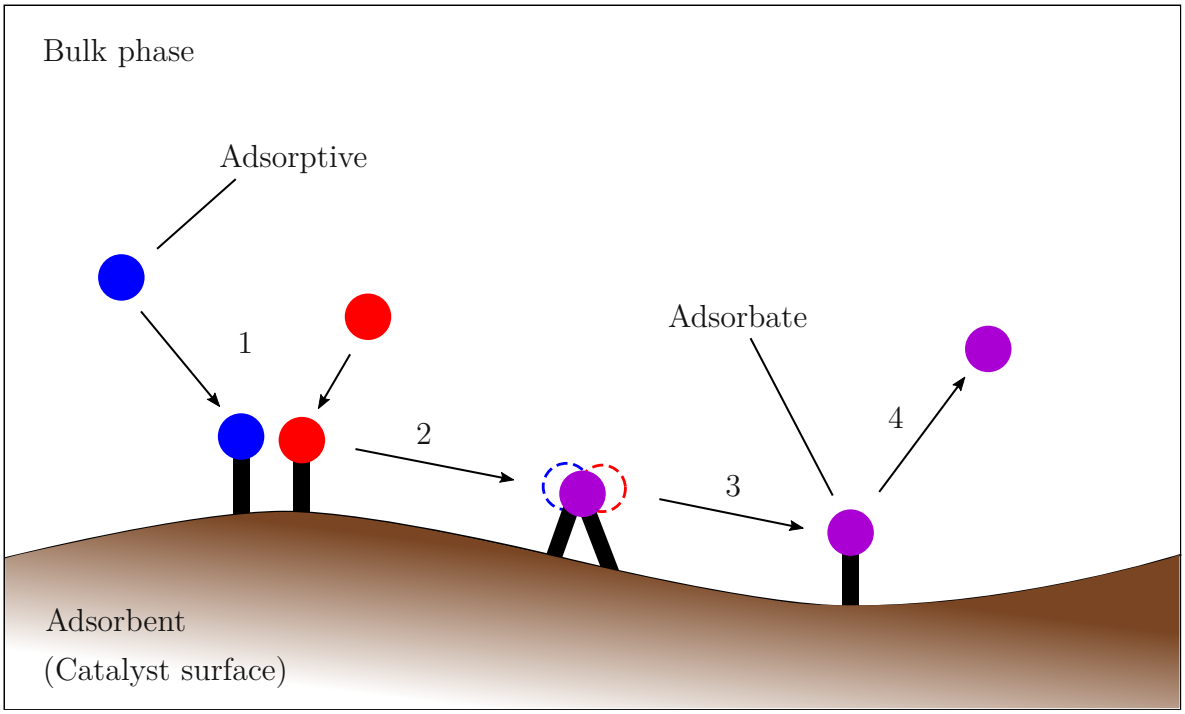

Figure 3.7: Scheme of the reaction sequence of a heterogeneously catalyzed reaction. 1= adsorption of the reactants; 2 and 3= reaction; 4= desorption

$$r_{CO} = \frac{dC_{CO}}{dt} = -k(T) \cdot C_{CO}. \tag{3.2}$$

Equation (3.2) shows that the first-order rate equation is fully described with just one concentration (in this case CO) and the rate constant $k(T)$. The H_2 concentration was not taken into account. Copp and Streeter further evaluated the rate constants, calculated from their experiments. A correlation between rate constant and space velocity was found. According to them, this effect could be caused by either an incorrect kinetic model, a non-uniform temperature distribution in the bed at low flow rates or mass transfer limitation at low flow rates. Due to the relatively small impact on their results, they made no effort to further investigate this problem [53].

3.4.2 Kinetics of heterogeneous catalysis

For the heterogeneous catalyzed methanation process, the adsorption and desorption process on a catalyst particle must also be taken into account, to describe the reaction kinetics accurately. Figure 3.7 shows how a heterogeneously catalysed reaction proceeds.

One possibility to describe heterogeneously catalyzed reactions mathematically is the Langmuir-Hinshelwood mechanism (LHM) [54]. The LHM splits a reaction into three steps: adsorption of the reactants, conversion into the product and desorption of the product. Each of the three reactions can proceed forwards, as well as backward. Let A, B and C be molecules involved in a heterogeneously catalyzed reaction and let S^* be a vacant site of the catalyst. Then the equilibrium can be written as

$$A + B + 2\,S^* \rightleftharpoons A - S^* + B - S^* \rightleftharpoons C - S^* + S^* \rightleftharpoons \text{product(C)} + 2\,S^*. \quad (3.3)$$

Adsorption or desorption is considered as any chemical equilibrium. However, the equilibrium does not exist between two reactants, but between molecules M and vacant sites of the catalyst S^*. The adsorption constant K can be written as

$$K = \frac{[S{-}M]}{\left[S^*\right] \cdot [M]}. \quad (3.4)$$

At this point the surface coverage Θ should be introduced as a new variable. It is often used to quantify adsorption processes. Θ describes the part of the catalyst surface, that is covered with an adsorbate.

$$\Theta = \frac{\text{Surface covered with adsorbate}}{\text{Whole amount of coverable surface sites}} \quad (3.5)$$

Considering (3.4), its obvious that the amount of sites occupied by molecules [S−M] is proportional to Θ. The amount of vacant sites $\left[S^*\right]$ is proportional to $(1 - \Theta)$ and the number of molecules [M] is proportional to the partial pressure p of the considered gas. Therefore, it can be said that

$$K(T) = C \cdot \frac{\Theta}{(1 - \Theta) \cdot p}, \quad (3.6)$$

where C is a constant. After rearrangements, (3.6) gives back the formula of the Langmuir-Hinshelwood isotherm, that describes the adsorption of a single gas species on the catalyst. Let $b(T)$ be a new adsorption constant described by $\frac{K(T)}{C}$, the Langmuir-Hinshelwood isotherm is written as

$$\Theta(T) = \frac{\frac{K(T)}{C} \cdot p}{1 + \frac{K(T)}{C} \cdot p} = \frac{b(T) \cdot p}{1 + b(T) \cdot p}. \quad (3.7)$$

Both reactants must adsorb on the catalyst surface for bimolecular reactions like the one in (3.3). Due to that, the number of free catalyst sites for bimolecular reactions is proportional to $(1 - \Theta_A - \Theta_B)$. For example, the surface coverage of component A is then written as

$$\Theta_{\mathrm{A}} = \frac{K_{\mathrm{A}} \cdot p_{\mathrm{A}}}{1 + K_{\mathrm{A}} \cdot p_{\mathrm{A}} + K_{\mathrm{B}} \cdot p_{\mathrm{B}}}. \tag{3.8}$$

For bimolecular reactions (A + B $\rightleftharpoons$ C) of ideal gases, the reaction rate r_C is given by the change of the partial pressure of the product C over time. It is further described by the partial pressures of the educts A & B and a rate constant k.

$$r_{\mathrm{C}} = \frac{dp_{\mathrm{C}}}{dt} = k \cdot p_{\mathrm{A}} \cdot p_{\mathrm{B}}. \tag{3.9}$$

However, only absorbed species can react with each other. Therefore, the partial pressures p in (3.9) are replaced by the surface coverage Θ of the components to get the reaction rate of heterogeneously catalyzed, bimolecular reactions (3.10).

$$r_{\mathrm{C}} = \frac{dp_{\mathrm{C}}}{dt} = k \cdot \Theta_{\mathrm{A}} \cdot \Theta_{\mathrm{B}} = k \cdot \frac{K_{\mathrm{A}} \cdot p_{\mathrm{A}} \cdot K_{\mathrm{B}} \cdot p_{\mathrm{B}}}{(1 + K_{\mathrm{A}} \cdot p_{\mathrm{A}} + K_{\mathrm{B}} \cdot p_{\mathrm{B}})^2}. \tag{3.10}$$

The rate constants k, as well as the adsorption constants K, can be formulated with the Arrhenius approach (3.1). However, in the equation for the adsorption constants, the activation energy E_A is replaced by the heat of adsorption ΔH [54, 52].

3.4.3 Rate equation models for CO-methanation and water-gas shift

In theory, reactions on catalysts, like CO-methanation or the water-gas shift reaction, can be described as a series of small reaction steps. To approximate the kinetics of such a system of follow-up reactions, it is enough to know the rate equation of the slowest reaction step. This rate-determining step is responsible for the overall rate of the reaction [9].

Kopyscinski et al. [9] studied the reaction mechanisms of CO-methanation and water-gas shift, with the idea to formulate rate equations for both reactions. In the study, two different reaction mechanisms of CO-methanation were investigated. Both mechanisms are thought to proceed via molecular adsorption of hydrogen and carbon monoxide. In the first mechanism, proposed by Araki and Ponec, a dissociation of CO follows the adsorption. Adsorbed carbon seems to be the intermediate. Together with hydrogen, it reacts stepwise to CH_4. The alternative mechanism would propose an oxygenated compound as an intermediate. An example would be that hydrogen reacts with CO to form a COH-complex. The C−O bond of the complex is cleaved more easily than the bond of carbon monoxide because it has a lower activation barrier. In an up-following step, the COH-complex either dissociates or reacts with hydrogen to form CH_y, which

reacts further to CH_4.

In the end, 16 different reaction steps were chosen as the possible rate-determining steps of the CO-methanation. Out of these steps, Kopyscinski et al. derived 32 rate equations (two per reaction step) and estimated parameters for each equation. A Langmuir-Hinshelwood approach was used to express the rate equations. The estimated parameters include the pre-exponential factors of the rate and adsorption coefficients, as well as the corresponding activation energies and heats of adsorption. The rate-determining step is assumed to be the one where the rate equation model gives the best fit to experimental data. Three models gave a better fit than the others and reflected the measured data equally well. One of these rate equations is given by

$$r_{\text{Methanation}} = \frac{k_1 \cdot K_{\text{CH}} \cdot p_{\text{CO}}^{0.5} \cdot p_{\text{H}_2}}{\left(1 + K_{\text{CH}} \cdot p_{\text{CO}}^{0.5} \cdot p_{\text{H}_2}^{0.5} + K_{\text{OH}} \cdot p_{\text{H}_2\text{O}} \cdot p_{\text{H}_2}^{-0.5}\right)^2}. \tag{3.11}$$

The corresponding rate-determining step would be $CH^* + H^* \longrightarrow CH_2^* + *$.
The rate-determining step of the water-gas shift reaction is assumed to be the reaction of the adsorbed species ($CO^* + OH^* \rightleftharpoons CO_2^* + H^*$). The rate equation for the water-gas shift reaction can be written as

$$r_{\text{WGS}} = \frac{k_2 \cdot \left(K_\alpha \cdot p_{\text{CO}} \cdot p_{\text{H}_2\text{O}} - \frac{p_{\text{CO}_2} \cdot p_{\text{H}_2}}{K_{\text{eq,WGS}}}\right)}{p_{\text{H}_2}^{0.5} \cdot \left(1 + K_{\text{CH}} \cdot p_{\text{CO}}^{0.5} \cdot p_{\text{H}_2}^{0.5} + K_{\text{OH}} \cdot p_{\text{H}_2\text{O}} \cdot p_{\text{H}_2}^{-0.5}\right)^2}. \tag{3.12}$$

K_α and k_2 are summarized parameters that contain the adsorption constants of the involved species. Additionally, k_2 contains the rate constant of the water-gas shift reaction.

Kopyscinski et al. [9] neglected the reverse reaction of the CO-methanation, due to the large equilibrium constant at low temperatures. In a later work, Witte et al. [55] changed the kinetic approach, published by Kopyscinski, to implement an equilibrium constant in the CO-methanation term. The new rate equation proposed by Witte can be written as

$$r_{\text{Methanation}} = \frac{k_1 \cdot K_{\text{C}} \cdot p_{\text{CO}}^{0.5} \cdot p_{\text{H}_2} \cdot \left(1 - \frac{p_{\text{CH}_4} \cdot p_{\text{H}_2\text{O}}}{K_{\text{eq,Meth}} \cdot p_{\text{CO}} \cdot p_{\text{H}_2}^3}\right)}{\left(1 + K_{\text{C}} \cdot p_{\text{CO}}^{0.5} \cdot p_{\text{H}_2}^{0.5} + K_{\text{OH}} \cdot p_{\text{H}_2\text{O}} \cdot p_{\text{H}_2}^{-0.5}\right)^2}. \tag{3.13}$$

The corresponding rate equation for the water-gas shift reaction is

$$r_{\mathrm{WGS}} = \frac{k_2 \cdot \left(K_\alpha \cdot p_{\mathrm{CO}} \cdot p_{\mathrm{H_2O}} - \frac{p_{\mathrm{CO_2}} \cdot p_{\mathrm{H_2}}}{K_{\mathrm{eq,WGS}}}\right)}{p_{\mathrm{H_2}}^{0.5} \cdot \left(1 + K_{\mathrm{C}} \cdot p_{\mathrm{CO}}^{0.5} \cdot p_{\mathrm{H_2}}^{0.5} + K_{\mathrm{OH}} \cdot p_{\mathrm{H_2O}} \cdot p_{\mathrm{H_2}}^{-0.5}\right)^2}. \tag{3.14}$$

Rönsch et al. [56] analyzed different rate equation models of the CO-methanation/ water-gas shift reaction system. The work aimed to find a suitable rate equation for wide temperature and pressure ranges. Rönsch states, that the kinetic approach, proposed by Kopyscinski (3.11) & (3.12), is only accurate for low temperatures (260-360 °C). To cover a wide temperature range Rönsch used models from Zhang [57] and Klose [58]. However, the models were adjusted to include backward reactions. The rate equations of the models are given below:

$$\begin{aligned} r_{\mathrm{Methanation}} = &- \frac{k_{1,\ \mathrm{Zhang/Klose}} \cdot K_{\mathrm{C}} \cdot K_{\mathrm{H}}^2 \cdot p_{\mathrm{CO}}^{0.5} \cdot p_{\mathrm{H_2}}}{\left(1 + K_{\mathrm{C}} \cdot p_{\mathrm{CO}}^{0.5} + K_{\mathrm{H}} \cdot p_{\mathrm{H_2}}^{-0.5}\right)^3} \\ &+ \frac{k_{1,\ \mathrm{Zhang/Klose}} \cdot K_{\mathrm{C}} \cdot K_{\mathrm{H}}^2 \cdot p_{\mathrm{CH_4}} \cdot p_{\mathrm{H_2O}} \cdot p_{\mathrm{CO}}^{-0.5} \cdot p_{\mathrm{H_2}}^{-2} \cdot \left(\frac{1}{K_{\mathrm{eq,Meth}}}\right)}{\left(1 + K_{\mathrm{C}} \cdot p_{\mathrm{CO}}^{0.5} + K_{\mathrm{H}} \cdot p_{\mathrm{H_2}}^{-0.5}\right)^3} \end{aligned} \tag{3.15}$$

$$r_{\mathrm{WGS}} = \frac{k_2 \cdot \left(p_{\mathrm{CO}} \cdot p_{\mathrm{H_2O}} - \frac{p_{\mathrm{CO_2}} \cdot p_{\mathrm{H_2}}}{K_{\mathrm{eq,WGS}}}\right)}{p_{\mathrm{H_2}} \cdot \left(1 + K_{\mathrm{CO}} \cdot p_{\mathrm{CO}} \cdot + K_{\mathrm{H_2}} \cdot p_{\mathrm{H_2}} + K_{\mathrm{CH_4}} \cdot p_{\mathrm{CH_4}} + \frac{K_{\mathrm{H_2O}} \cdot p_{\mathrm{H_2O}}}{p_{\mathrm{H_2}}}\right)^2} \tag{3.16}$$

Klose developed the rate equation for a catalyst with 18 mass% nickel supported on aluminium. Zhang modified the parameters in the rate equation, proposed by Klose. This resulted in rate equations for a 50 mass% nickel catalyst. Therefore in (3.15), the rate coefficient k_1 changes with different catalysts [56].

3.5 Kinetic plant model

This section shows how the product gas conversion inside the ICFB reactor is modeled. It presents necessary parameters and assumptions as well as all the equations that are used.

3.5.1 Model structure

In this work, a two-phase approach is used to model the fluidized bed. The model is derived from Kopyscinski et al. [9]. Additionally to the original two-phase model described in Section 3.2.2, this model considers the bubble growth through the bed and the volume contraction during the reaction. Figure 3.8 shows a scheme of the two-phase model.

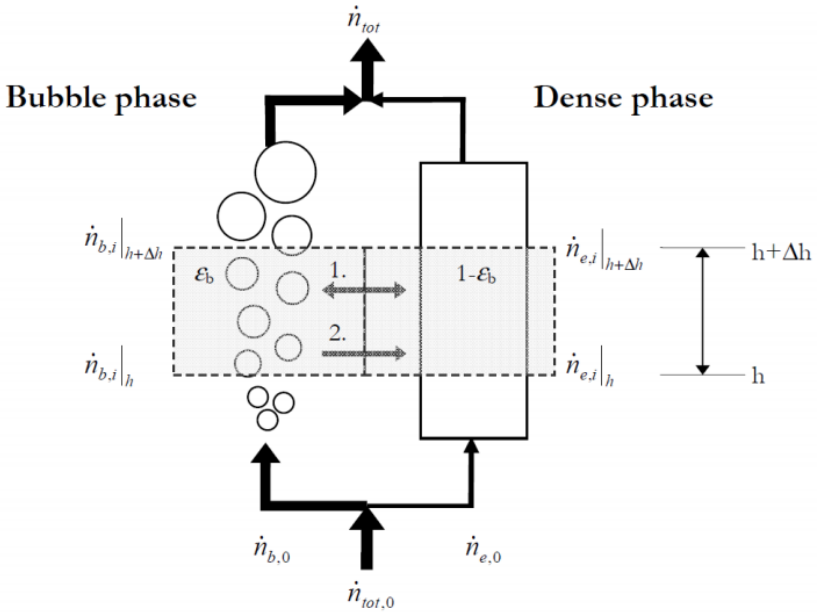

Figure 3.8: Scheme of a two phase fluidized bed model with 1. mass transfer due to the concentration gradient between both phases and 2. convective mass flow (bulk flow) due to the volume contraction in the dense phase [9].

Assumptions

To further simplify the mathematical model, the following assumptions are made:

- The reactor is in a steady-state and all gases behave ideally.
- Bubbles are solid free. No reactions take place in the bubble phase, due to the absence of catalyst particles.
- Possible influence of pore diffusion is neglected. Concentration on and in the catalyst particles is the same as in the dense phase.
- Ideal plug flow prevails inside the fluidized bed. No axial dispersion takes place. Radial concentration differences are neglected.
- Pressure loss due to the weight of the solid is neglected.
- No carbon deposition takes place on the catalyst.
- The gas flow rate through the dense phase is constant.
- Due to the volume contraction during the reaction, it is necessary to provide an additional convective mass transfer between the dense and the bubble phase, to maintain the constant flow rate in the dense phase. This bulk flow proceeds immediately at the height where the molar reduction occurs.
- The temperature through the fluidized bed is constant.
- Catalyst particles are spherical.
- The weight hourly space velocity (WHSV) is the same for both, the annular region and the draft tube.
- No reactions take place in the freeboard

General equations

As stated in Section 3.5.1, the gas velocity in both sections of the ICFB reactor is the same. Therefore both sections are combined in the model. The combined cross-section A_{Reactor} is given by

$$A_{\text{Reactor}} = \left(d_{\text{dt}}^2 + d_{\text{ar,o}}^2 - d_{\text{ar,i}}^2\right) \cdot \frac{\pi}{4}. \tag{3.17}$$

Furthermore, the bed volume V_{b} can be calculated by multiplying the reactor cross-section with the bed height h_{b}

$$V_{\mathrm{b}} = A_{\mathrm{Reactor}} \cdot h_{\mathrm{b}} \tag{3.18}$$

Let the volume of the particles V_{p} be the quotient of catalyst mass m_{cat} and ρ_{cat}. Then, the porosity ε of the catalyst bed is given by

$$\varepsilon = 1 - \frac{V_{\mathrm{p}}}{V_{\mathrm{b}}} = 1 - \frac{m_{\mathrm{cat}}}{\rho_{\mathrm{cat}} \cdot V_{\mathrm{b}}}. \tag{3.19}$$

Assuming Geldart B particles, the bed expansion at u_{mf} is negligible and the porosity ε is assumed to be the porosity at the point of minimum fluidization $\varepsilon_{\mathrm{mf}}$.
u_{mf} is calculated via the Archimedes number Ar as it is shown in [7]. The Archimedes number is given by

$$Ar = \frac{\rho_{\mathrm{g}} \cdot d_{\mathrm{cat}}^3 \cdot (\rho_{\mathrm{cat}} - \rho_{\mathrm{g}}) \cdot g}{\mu^2}, \tag{3.20}$$

where μ is the dynamic viscosity of the gas mixture inside the reactor, d_{cat} is the diameter of a catalyst particle, g is the acceleration due to gravity and ρ_{g} is the density of the gas mixture inside the reactor. ρ_{g} is calculated with data and equations from VDI heat atlas [59]. μ is calculated after Wilke et al. [60] and with data from DIPPR. u_{mf} is written as

$$u_{mf} = \frac{\mu}{\rho_{\mathrm{g}} \cdot d_{\mathrm{cat}}} \left(\sqrt{33.7^2 + 0.0408 \cdot Ar} - 33.7 \right). \tag{3.21}$$

The relationship between weight hourly space velocity $WHSV$ and standard volumetric flow rate $\dot{V}_{\mathrm{N}}$ is given by

$$\dot{V}_{\mathrm{N}} = WHSV \cdot m_{\mathrm{cat}}. \tag{3.22}$$

From $\dot{V}_{\mathrm{N}}$, it is possible to calculate the superficial gas velocity u and the molar flow rate $\dot{n}$. Let $T_0 = 273.15\,K$ be the standard temperature and $p_0 = 101325\,Pa$ be the standard pressure. Then

$$u = \frac{\dot{V}_{\mathrm{N}} \cdot T}{T_0 \cdot A_{\mathrm{Reactor}} \cdot 3600} \tag{3.23}$$

and

$$\dot{n} = \frac{\dot{V}_{\mathrm{N}} \cdot p_0}{R \cdot T_0 \cdot 3600}. \tag{3.24}$$

The gas flow through the dense phase $\dot{V}_{\mathrm{e}}$ is assumed to be constant and flows at u_{mf}. If the total gas flow is higher than $\dot{V}_{\mathrm{e}}$, the surplus gas rises in bubbles at excess gas velocity $v_{\mathrm{b}} = (u - u_{\mathrm{mf}})$. Therefore the total gas flow can be divided as follows.

$$\dot{V} = \dot{V}_{\mathrm{e}} + \dot{V}_{\mathrm{b}} = A_{\mathrm{Reactor}} \cdot u_{\mathrm{mf}} + A_{\mathrm{Reactor}} \cdot (u - u_{\mathrm{mf}}), \tag{3.25}$$

where $\dot{V}$ is the total gas flow and $\dot{V}_{\mathrm{b}}$ describes the gas flow through the bubble phase.

Bubble growth

This model considers bubble growth throughout the catalyst bed. A bubble growth correlation proposed by Werther [61] is used in this model. Let $d_{\mathrm{b}}(h)$ be the diameter of the bubbles in the fluidized bed estimated at a bed height h. Then, the bubble growth correlation for Geldart B particles is given by

$$d_{\mathrm{b}}(h) = 0.00853 \cdot (1 + 27.2 \cdot (u - u_{\mathrm{mf}}))^{\frac{1}{3}} \cdot (1 + 6.84 \cdot h)^{1.21}. \tag{3.26}$$

The velocity of the rise of a crowd of bubbles $u_{\mathrm{b}}(h)$ given by Davidson and Harrison, written in [46] is described as

$$u_{\mathrm{b}}(h) = (u - u_{\mathrm{mf}}) + 0.711 \cdot \sqrt{g \cdot d_{\mathrm{b}}(h)}. \tag{3.27}$$

The quotient of excess gas velocity $v_{\mathrm{b}} = (u - u_{\mathrm{mf}})$ and $u_{\mathrm{b}}(h)$ gives the height dependent bubble gas hold-up.

$$\varepsilon_{\mathrm{b}}(h) = \frac{v_{\mathrm{b}}}{u_{\mathrm{b}}(h)}. \tag{3.28}$$

Molar balances

For every gaseous compound i in the methanation reactor, two molar balances must be considered:

Molar balance of the dense/emulsion phase:

$$\frac{\partial \dot{n}_{\mathrm{e,i}}}{\partial h} = -K_{\mathrm{G,i}} \cdot a \cdot A_{\mathrm{Reactor}} \cdot (c_{\mathrm{b,i}} - c_{\mathrm{e,i}}) - \dot{N}_{\mathrm{vc}} \cdot x_{\mathrm{b,i}} + (1 - \varepsilon_{\mathrm{b}}) \cdot (1 - \varepsilon_{\mathrm{mf}}) \cdot \rho_{\mathrm{cat}} \cdot A_{\mathrm{Reactor}} \cdot R_{\mathrm{i}} \tag{3.29}$$

Molar balance of the bubble phase:

$$\frac{\partial \dot{n}_{\mathrm{b,i}}}{\partial h} = +K_{\mathrm{G,i}} \cdot a \cdot A_{\mathrm{Reactor}} \cdot (c_{\mathrm{b,i}} - c_{\mathrm{e,i}}) + \dot{N}_{\mathrm{vc}} \cdot x_{\mathrm{b,i}} \tag{3.30}$$

The molar balances consist of different mathematical terms that are described in more detail below. Only the molar balances for the dense phase (3.29) contain a reaction therm since no reactions are assumed to happen in the bubble phase. The mass exchange between the two phases is considered by a mass transfer therm and a bulk flow therm.

Mass transfer

The mass transfer therm is given by

$$K_{\mathrm{G,i}} \cdot a \cdot A_{\mathrm{Reactor}} \cdot (c_{\mathrm{b,i}} - c_{\mathrm{e,i}}) \,, \tag{3.31}$$

where $c_{\mathrm{b,i}}$ and $c_{\mathrm{b,i}}$ are the concentrations of the component i in the bubble and dense phase. $K_{\mathrm{G,i}}$ is the mass transfer coefficient for the respective gas species i. The driving force for the mass transfer is the concentration difference between both phases. The mass transfer coefficients for the gases are calculated after Sit and Grace [62]. Let D_{i} be the diffusion coefficient of the gas component i. Then,

$$K_{\mathrm{G,i}} = \frac{u_{\mathrm{mf}}}{3} + \sqrt{\frac{4 \cdot D_{\mathrm{i}} \cdot \varepsilon_{\mathrm{mf}} \cdot u_{\mathrm{b}}}{\pi \cdot d_{\mathrm{b}}}}. \tag{3.32}$$

The calculation of D_{i} is made according to Wilke and Lee [63]. Atomic diffusion volumes to calculate D_{i} are taken from Fuller et al. [64, 65].
Lastly, the mass transfer is affected by the mass transfer surface area between bubble and dense phase. Inside a height differential, the mass transfer surface area is the product of A_{Reactor} and the specific surface area of spherical bubbles per unit fluidized bed volume a. Further, a is written as

$$a = \frac{6 \cdot \varepsilon_{\mathrm{b}}}{d_{\mathrm{b}}}. \tag{3.33}$$

Bulk flow

Equations (3.29) and (3.30) include the bulk flow therm $\dot{N}_{\mathrm{vc}} \cdot x_{\mathrm{b,i}}$, where $\dot{N}_{\mathrm{vc}}$ is the bulk flow between the bubble and the dense phase and $x_{\mathrm{b,i}}$ is the volume fraction of the gas species in the bubble phase. Kopyscinski introduced it to the model to cover up molar losses due to the non equimolar reaction and mass transfer to the dense phase [9]. The bulk flow is calculated by

$$\dot{N}_{\mathrm{vc}} = \frac{\partial \dot{n}_{\mathrm{vc}}}{\partial h} = \sum_i K_{\mathrm{G,i}} \cdot a \cdot A_{\mathrm{Reactor}} \cdot (c_{\mathrm{b,i}} - c_{\mathrm{e,i}}) + (1 - \varepsilon_{\mathrm{b}}) \cdot (1 - \varepsilon_{\mathrm{mf}}) \cdot \rho_{\mathrm{cat}} \cdot A_{\mathrm{Reactor}} \cdot \sum_i R_{\mathrm{i}}, \tag{3.34}$$

where R_{i} is the rate of formation (or disappearance).

The reaction system

Although other reactions are occurring during the methane synthesis, four reactions have been regarded as the most influential. CO-methanation (2.1), CO_2-methanation

Table 3.2: Reaction system used for thermodynamic calculations

Reaction	Name
$CO + 3\,H_2 \rightleftharpoons CH_4 + H_2O$	CO-methanation
$CO + H_2O \rightleftharpoons CO_2 + H_2$	Water-gas-shift reaction

(2.3) the water-gas shift reaction (2.2) and hydrogenation of ethylene (2.4). Other reactions are neglected in the calculations of this work. For the hydrogenation of ethylene, it is assumed that the usually small amounts of ethylene in the product gas are fully hydrogenated during methane synthesis. This allows the pre-calculation of the expected reaction yields. Let $\dot{n}_\mathrm{i}$ and $\dot{n}_\mathrm{i,new}$ be the molar flow rates before and after the pre-calculation, respectively. Then,

$$\dot{n}_{\mathrm{H_2,new}} = \dot{n}_{\mathrm{H_2}} - 2\dot{n}_{\mathrm{C_2H_4}}, \qquad \dot{n}_{\mathrm{CH_4,new}} = \dot{n}_{\mathrm{CH_4}} + 2\dot{n}_{\mathrm{C_2H_4}} \qquad \textit{and} \qquad \dot{n}_{\mathrm{C_2H_4,new}} = 0. \tag{3.35}$$

Considering, that CO_2-methanation is a linear combination of CO-methanation and the water-gas shift reaction, and the pre-calculation of the ethylene hydrogenation, the final reaction system can be shortened to only two reactions. Table Table 3.2 displays the final reaction system.

Chemical Equilibrium

As reactions always proceed in the direction where the Gibbs free energy decreases, the equilibrium point of a reaction system is defined at the minimum of the Gibbs free energy function. Gibbs free energy $G(p,T)$ is pressure and temperature-dependent and is written as

$$G(p,T) = U + p \cdot V - T \cdot S = H - T \cdot S, \tag{3.36}$$

where U is the inner energy of a system, S is the entropy and H is the enthalpy. At atmospheric pressure, entropies and enthalpies of the reactants in Table 3.2 can be calculated by using the NASA polynomials. They approximate isobaric heat capacity c_p, enthalpy H and entropy S for different species at different temperatures. The coefficients a_n are given by [66].

$$\frac{c_\mathrm{p}}{R} = a_1 + a_2 \cdot T + a_3 \cdot T^2 + a_4 \cdot T^3 + a_5 \cdot T^4. \tag{3.37}$$

$$\frac{H}{R \cdot T} = a_1 + \frac{a_2 \cdot T}{2} + \frac{a_3 \cdot T^2}{3} + \frac{a_4 \cdot T^3}{4} + \frac{a_5 \cdot T^4}{5} + \frac{a_6}{T}. \tag{3.38}$$

$$\frac{S}{R} = a_1 \cdot ln(T) + a_2 \cdot T + \frac{a_3 \cdot T^2}{2} + \frac{a_4 \cdot T^3}{3} + \frac{a_5 \cdot T^4}{4} + a_7. \tag{3.39}$$

The Gibbs free energy of reaction at standard pressure $\Delta G^0_{\mathrm{R}}(T)$ is then formed by combining conventional enthalpies and entropies of the participating species. Let ν_{i} be the stoichiometric factor of the considered reaction, which has positive values for products and negative values for educts. Then,

$$\Delta G^0_{\mathrm{R}}(T) = \sum_i \left[\nu_{\mathrm{i}} \cdot H_{\mathrm{i}}\left(p_0, T\right)\right] - T \cdot \sum_i \left[\nu_{\mathrm{i}} \cdot S_{\mathrm{i}}\left(p_0, T\right)\right]. \tag{3.40}$$

Assuming ideal gas behaviour, the equilibrium constant for partial pressures K_{P} is a function of $\Delta G^0_{\mathrm{R}}(T)$ and T. Furthermore, K_{P} can also be formed as the dimensionless product of the partial pressure of the reactants p_{i} relative to standard pressure p_0.

$$K_{\mathrm{P}}(T) = e^{-\frac{\Delta G^0_{\mathrm{R}}(T)}{R \cdot T}} = \prod_i \left(\frac{p_{\mathrm{i}}}{p_0}\right)^{\nu_{\mathrm{i}}}. \tag{3.41}$$

According to Dalton's law, the partial pressures of the gases in the mixture are given by

$$p_{\mathrm{i}} = p \cdot \left(\frac{\dot{n}_{\mathrm{i}}}{\sum \dot{n}_{\mathrm{i}}}\right) = p \cdot y_{\mathrm{i}}, \tag{3.42}$$

where y_{i} is the molar fraction of a gas component i. The equilibrium constant can take values from zero to infinity and shows the equilibrium point of a chemical reaction. The chemical equilibrium of a reaction tends to the educt side for small values of K_P, whereas for large values of K_P the product side is favored.

Assuming isobaric and isothermal behavior in the reactor, it is possible to fully describe the reaction system with five equations. Three element balances and the equilibrium formulations for the respective reactions [67]:

1. C balance $\left(\frac{\mathrm{mol_C}}{\mathrm{s}}\right)$:

$$\dot{n}_{\mathrm{CH_4,in}} + \dot{n}_{\mathrm{CO,in}} + \dot{n}_{\mathrm{CO_2,in}} = \dot{n}_{\mathrm{CH_4,out}} + \dot{n}_{\mathrm{CO,out}} + \dot{n}_{\mathrm{CO_2,out}} \tag{3.43}$$

2. H_2 balance $\left(\frac{\mathrm{mol_{H_2}}}{\mathrm{s}}\right)$:

$$2 \cdot \dot{n}_{\mathrm{CH_4,in}} + \dot{n}_{\mathrm{H_2,in}} + \dot{n}_{\mathrm{H_2O,in}} = 2 \cdot \dot{n}_{\mathrm{CH_4,out}} + \dot{n}_{\mathrm{H_2,out}} + \dot{n}_{\mathrm{H_2O,out}} \tag{3.44}$$

3. O balance $\left(\frac{\mathrm{mol_O}}{\mathrm{s}}\right)$:

$$2 \cdot \dot{n}_{\mathrm{CO_2,in}} + \dot{n}_{\mathrm{CO,in}} + \dot{n}_{\mathrm{H_2O,in}} = 2 \cdot \dot{n}_{\mathrm{CO_2,out}} + \dot{n}_{\mathrm{CO,out}} + \dot{n}_{\mathrm{H_2O,out}} \tag{3.45}$$

4. Equilibrium methanation:

$$K_{\mathrm{P,meth}} = y_{\mathrm{CH_4,out}} \cdot y_{\mathrm{H_2O,out}} \cdot \left(y_{\mathrm{H_2,out}}\right)^{-3} \cdot \left(y_{\mathrm{CO,out}}\right)^{-1} \cdot \left(\frac{p}{p_0}\right)^{-2} \tag{3.46}$$

5. Equilibrium water-gas-shift:

$$K_{\mathrm{P,wgs}} = y_{\mathrm{CO_2,out}} \cdot y_{\mathrm{H_2,out}} \cdot \left(y_{\mathrm{H_2O,out}}\right)^{-1} \cdot \left(y_{\mathrm{CO,out}}\right)^{-1} \tag{3.47}$$

This system of non-linear equations is solved with numerical methods. To represent the conditions of the investigated reactor, the calculation is done for atmospheric pressure and temperatures between 270 and 420 °C. The obtained solution yields the molar flow rates of each involved species at equilibrium conditions. For this work, a built-in Matlab function from the *optimization toolbox* [68], called "fsolve" is used to solve the equation system.

Another method to estimate the equilibrium is the relaxation method by Baerns et al. [69]. For this method, the reaction system is split up into a series of single reactions. It is assumed that every reaction takes place in an individual reactor, where it reaches equilibrium. Let Δn describe the change in the number of moles for every species involved. Then the molar balances can be written as follows:

$$\mathrm{CH_4} : n_{\mathrm{CH_4},out} = n_{\mathrm{CH_4},in} + \Delta n \qquad \mathrm{H_2O} : n_{\mathrm{H_2O},out} = n_{\mathrm{H_2O},in} + \Delta n$$
$$\mathrm{CO} : n_{\mathrm{CO},out} = n_{\mathrm{CO},in} - \Delta n \qquad \mathrm{H_2} : n_{\mathrm{H_2},out} = n_{\mathrm{H_2},in} - 3 \cdot \Delta n$$
$$\sum_i n_{i,out} = \sum_i n_{i,in} - 2 \cdot \Delta n$$

The equilibrium in each reactor is then calculated with the respective equilibrium constant K_{P}. As example, for the CO-methanation $K_{\mathrm{P,meth}}$ is given by

$$K_{\mathrm{P,meth}} = \frac{y_{\mathrm{CH_4,out}} \cdot y_{\mathrm{H_2O,out}}}{y_{\mathrm{H_2,out}}^3 \cdot y_{\mathrm{CO,out}}} \cdot \left(\frac{p}{p_0}\right)^{-2} = \frac{n_{\mathrm{CH_4,out}} \cdot n_{\mathrm{H_2O,out}} \cdot \left(\sum n_{\mathrm{i,out}}\right)^2}{n_{\mathrm{H_2,out}}^3 \cdot n_{\mathrm{CO,out}}} \cdot \left(\frac{p}{p_0}\right)^{-2}. \tag{3.48}$$

Inserting the molar balances, the following equation is obtained.

$$K_{\mathrm{P,meth}} = \frac{\left(n_{\mathrm{CH_4,in}} + \Delta n\right) \cdot \left(n_{\mathrm{H_2O,in}} + \Delta n\right) \cdot \left(\sum n_{\mathrm{i,in}} - 2 \cdot \Delta n\right)^2}{\left(n_{\mathrm{H_2,in}} - 3 \cdot \Delta n\right)^3 \cdot \left(n_{\mathrm{CO,in}} - \Delta n\right)} \cdot \left(\frac{p}{p_0}\right)^{-2} \tag{3.49}$$

By solving the equation for Δn and inserting it back into the molar balances, a new equilibrium composition is calculated. The gas with the new composition then enters

the next reactor. As one can see, the calculation is an iterative process. During the process, Δn gets smaller with every new iteration step. The calculation stops when Δn is smaller than a set tolerance.

Rate equation

In this work, the different rate equation models from Section 3.4.3 are investigated. Therefore, the reaction rates of methanation $r_{\text{Methanation}}$ and water-gas shift r_{WGS} are converted into rates of formation (or disappearance) R_{i} and are then implemented in the overall model of the fluidized-bed reactor. The rates of formation of the different species, that are part of the reaction system shown in Table 3.2, are formulated out of the reaction rates as follows:

$$
\begin{aligned}
R_{\text{H}_2} &= -3 \cdot r_{\text{Methanation}} + r_{\text{WGS}} \\
R_{\text{CO}} &= -r_{\text{Methanation}} - r_{\text{WGS}} \\
R_{\text{CO}_2} &= r_{\text{WGS}} \\
R_{\text{CH}_4} &= r_{\text{Methanation}} \\
R_{\text{H}_2\text{O}} &= r_{\text{Methanation}} - r_{\text{WGS}}
\end{aligned}
$$

The parameters for the calculations of the rate and adsorption constants are directly taken out of the respective works of Kopyscinski, Witte and Rönsch [20, 55, 56]. Table 3.3 shows how adsorption and rate constants are calculated. Rönsch used an Arrhenius approach to calculate the rate and adsorption parameters. In the Arrhenius approach, pre-exponential factors often have high values, since they refer to infinite temperature. Kopyscinski and Witte defined a finite reference temperature T_{ref} at 325 °C. Due to that, they were able to modify the Arrhenius approach and decrease the magnitudes of the pre-exponential factors. Table A.4 in Appendix A shows the parameter values that are used for the different rate equation models.

Additionally to the rate equations of Section 3.4.3, a new rate equation for the water-gas shift reaction is formed. The new rate equation has the purpose to satisfy the thermodynamic equilibrium of the gas phase, which could not be reached by (3.12). This is accomplished, by simply setting the value of K_α, in (3.14), to a constant value of 1. The modified rate equation is given by

$$
r_{\text{WGS}} = \frac{k_2 \cdot \left(p_{\text{CO}} \cdot p_{\text{H}_2\text{O}} - \frac{p_{\text{CO}_2} \cdot p_{\text{H}_2}}{K_{\text{eq,WGS}}} \right)}{p_{\text{H}_2}^{0.5} \cdot \left(1 + K_{\text{C}} \cdot p_{\text{CO}}^{0.5} \cdot p_{\text{H}_2}^{0.5} + K_{\text{OH}} \cdot p_{\text{H}_2\text{O}} \cdot p_{\text{H}_2}^{-0.5} \right)^2}. \tag{3.50}
$$

Table 3.3: Calculation methods used by different researchers, to calculate the rate and adsorption constants in their respective models

	rate constant	adsorption constant
Rönsch	$k = k_0 \cdot e^{-\frac{E_A}{R \cdot T}}$	$K = K_0 \cdot e^{-\frac{\Delta H}{R \cdot T}}$
Kopyscinski	$k = e^{ln(k_0)} \cdot e^{\frac{E_A}{R \cdot T_{ref}} \cdot \left(1 - \frac{T_{ref}}{T}\right)}$	$K = e^{ln(K_0)} \cdot e^{\frac{\Delta H}{R \cdot T_{ref}} \cdot \left(1 - \frac{T_{ref}}{T}\right)}$
Witte	$k = k_0 \cdot e^{\frac{E_A}{R \cdot T_{ref}} \cdot \left(1 - \frac{T_{ref}}{T}\right)}$	$K = K_0 \cdot e^{\frac{\Delta H}{R \cdot T_{ref}} \cdot \left(1 - \frac{T_{ref}}{T}\right)}$

This modification of the rate equations proposed by Witte is investigated alongside the other rate equation models. The related parameters can be found in Table A.4 under *Witte**.

3.5.2 Parameter fitting

To optimize simulation results, models can be fitted to measured data. Previously chosen parameters are changed to minimize an optimization criterion. In the case of this work, the optimization criteria is given by the sum of the squared distances between the measured data points and the respective simulation results. Let $\boldsymbol{y}$ be a vector that contains the simulated molar fractions of the raw-SNG components at the reactor outlet and $\boldsymbol{y}_{\text{Measured}}$ are the corresponding measured data. Then, the cost function $J(\boldsymbol{\Theta})$, which must be minimized is given by

$$J(\boldsymbol{\Theta}) = \sum (\boldsymbol{y}(\boldsymbol{\Theta}) - \boldsymbol{y}_{\text{Measured}})^2, \tag{3.51}$$

where $\boldsymbol{\Theta}$ is a vector containing the parameters, that will be estimated. Zhang et al. [57] used already existing rate equation models and estimated new kinetic parameters. The same was done in this work. Out of the investigated rate equation models from Section 3.5.1, the most suitable model is taken and fitted to available data. Taking Zhang as an example, the adsorption parameters of the considered rate equation models are maintained. This leaves two changeable parameters per reaction, namely the pre-exponential factor k_0 and the activation energy E_A. Ultimately $\boldsymbol{\Theta}$ is written as

$$\boldsymbol{\Theta} = [k_{0,\text{WGS}} \quad E_{A,\text{WGS}} \quad k_{0,\text{Meth}} \quad E_{A,\text{Meth}}]^{\boldsymbol{T}}. \tag{3.52}$$

A quality criterion for the new model is given by the coefficient of determination R^2. Let SSE be the sum of squared errors of prediction and SST be the total sum of squares. Then,

$$R^2 = 1 - \frac{SSE}{SST}. \tag{3.53}$$

SSE and SST are defined by

$$SSE = \sum_{i=1}^{n} (y_i - \hat{y}_i)^2 \tag{3.54}$$

and

$$SST = \sum_{i=1}^{n} (y_i - \bar{y})^2, \tag{3.55}$$

where n is the number of measured values, y_i are the measured values of an experiment, $\hat{y}_i$ are the results of the corresponding simulation and $\bar{y}$ is the arithmetic mean value of the total measured values.

3.6 Thermal plant model

A nonlinear first-order differential equation is assumed to describe the dynamic behavior of the temperature inside the air-cooled reactor. The differential equation is identified, by setting up a heat balance around the fluidized bed and estimating unknown parameters under consideration of data gathered during an experiment with the ICFB reactor.

3.6.1 Heat balance

Figure 3.9 shows a scheme of the ICFB reactor and the energy flows into and out of the system boundaries. The change of the heat quantity inside the reactor $\frac{dQ}{dt}$ is given by

$$\frac{dQ}{dt} = \dot{Q}_{\text{reaction}} - \dot{Q}_{\text{air}} - \dot{Q}_{\text{loss}}, \tag{3.56}$$

where $\dot{Q}_{\text{air}}$ is the heat dissipated to the cooling air and $\dot{Q}_{\text{loss}}$ is the heat dissipated to the environment. The heat generated during the reaction $\dot{Q}_{\text{reaction}}$ is given by the difference of the enthalpies of the product gas $\dot{H}_{\text{in}}$ and the raw-SNG $\dot{H}_{\text{out}}$. Let there be a gas, consisting of n different gas species. Then,

$$\dot{H}_{\text{gas}}(T) = \sum_{i=1}^{n} \left(\dot{n}_i(T) \cdot h_i(T)\right), \tag{3.57}$$

where $\dot{H}_{\text{gas}}(T)$ is the enthalpy of the gas, $\dot{n}_i(T)$ is the molar flow of the gas species i and $h_i(T)$ is the specific enthalpy of a gas species i. The specific enthalpy of a gas species

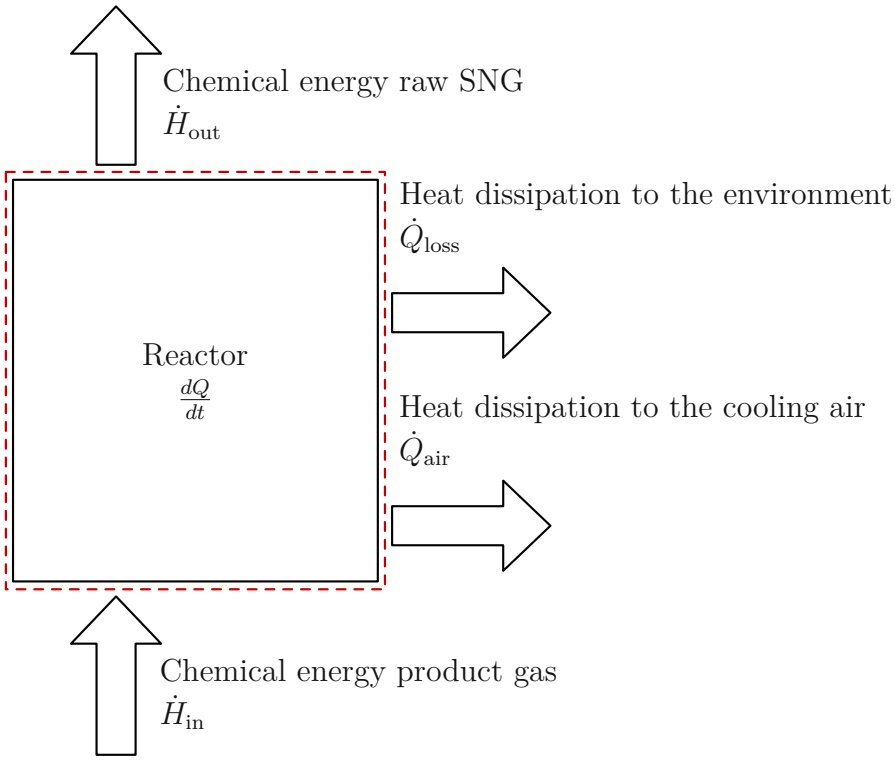

Figure 3.9: Heat balance of the reactor.

can be understood as the energy, that the species has in its actual state. It is composed of the standard enthalpy of formation of the species and the energy that is required to reach the actual state. The latter can take a positive or negative value, as it depends on the temperature and the pressure in which the species is present [67].

It should be noted, that the raw-SNG composition as well as $\dot{Q}_{\text{reaction}}$ are simulation results of the model in Section 3.5. The reaction heat $\dot{Q}_{\text{reaction}}$ is nonlinear and is calculated by solving the differential equations over the reactor hight h_{b} at a certain time t and a certain temperature $T_{Reactor}$. The dynamics inside the reactor are very fast compared to the temperature change of the reactor. Therefore, time dependencies of the raw-SNG composition can be neglected in the calculation.

Let ΔT be the difference between T_{Reactor} and the ambient air temperature T_{U}. Assuming that $\dot{Q}_{\text{loss}}$ is proportional to ΔT and $\dot{Q}_{\text{air}}$ is proportional to ΔT and the cooling airflow $\dot{V}_{\text{air}}$, the heat balance can alternatively be written as

$$\frac{dT_{\text{Reactor}}}{dt} = \frac{\dot{Q}_{\text{reaction}}(T_{\text{Reactor}}) - (T_{\text{Reactor}} - T_{\text{U}}) \cdot C_1 - (T_{\text{Reactor}} - T_{\text{U}}) \cdot \dot{V}_{\text{air}} \cdot C_2}{C_3}, \quad (3.58)$$

where C_{1-3} are proportional factors that contain constant parameters such as masses, surface areas, heat capacities, or heat transfer coefficients. In this model, T_{U} is assumed constant at 25 °C.

3.6.2 Experiment and parameter estimation

The unknown parameters C_{1-3} in (3.56) are estimated by fitting them to data, which were gathered in experiments. The experiments were executed in the ICFB reactor mentioned in Section 3.1. The reactor was preheated with nitrogen until operation conditions were met. Then, the nitrogen was slowly substituted with H_2, CO, CO_2, CH_4 and steam, to replicate product gas. The volume flows of the gas components were manually set. To provide steam, water was dosed via peristaltic pumps and then vaporized. The final feed gas composition was verified with a Rosemount NGA-2000 gas analyzer. The gas analyzer measures only the dry gas composition. Steam had to be condensed and removed before the gas was analyzed. The measurement device is designed for a single gas stream and can not measure the product gas and the raw-SNG simultaneously. Therefore the product gas composition wasn't adjusted after the start of the experiments and was assumed to be constant. Throughout the experiments, the gas analyzer was then used to monitor the raw-SNG composition.

Three experiments were conducted. One with a cooling air pressure of 5 bar, the other two with a cooling air pressure of 2.2 bar. Tables A.1-A.3 in Appendix A show the wet and dry feed gas compositions, the cooling air pressure and the pump settings of the respective experiments. To analyze the temperature behavior of the cooled reactor, the airflow in the cooling system was varied. The cooling airflow is controlled via the control valve opening percentages of the coil and the annular region. Both valves were always opened by the same percentage. Characteristic curves of the valves at 2.2 and 5 bar were estimated. With them, the valve opening percentage can be transformed into a volume flow, which makes it possible to compare the experiments to each other. The reactor temperature T_{Reactor} is the average of the measured temperatures inside the catalyst bed.

Starting from a defined operation point, the valve positions were slightly varied. When the reactor temperature reached a steady-state, the valve positions were changed back to the operating point. This procedure was repeated several times while changing the distance to the operating point. The exact valve positions that were set in the experiments are shown in Figures B.1 and B.2 in Appendix B.

The sampling rate during the experiment was 1 Hz. The signal was filtered with a moving average filter, with a set window size of 100. Then, a re-sampling was carried out, to shorten the calculation time of the parameter estimation. The new sampling rate was set at 0.01 Hz. The gathered data were then split into two data sets, one for parameter estimation and the second for cross-validation. The cost function $J(\boldsymbol{\Theta})$ used for parameter estimation is the same as the one in Section 3.5.2. The parameter vector $\boldsymbol{\Theta}$ is written as

$$\boldsymbol{\Theta} = [C_1 \quad C_2 \quad C_3]^{\boldsymbol{T}}, \tag{3.59}$$

where C_{1-3} are the parameters in the heat balance (3.58).

3.7 Results and discussion

The result section includes the characterization of the catalyst class, the evaluation of the thermodynamic equilibrium models and both reactor models. Both of the reactor models were cross-validated.

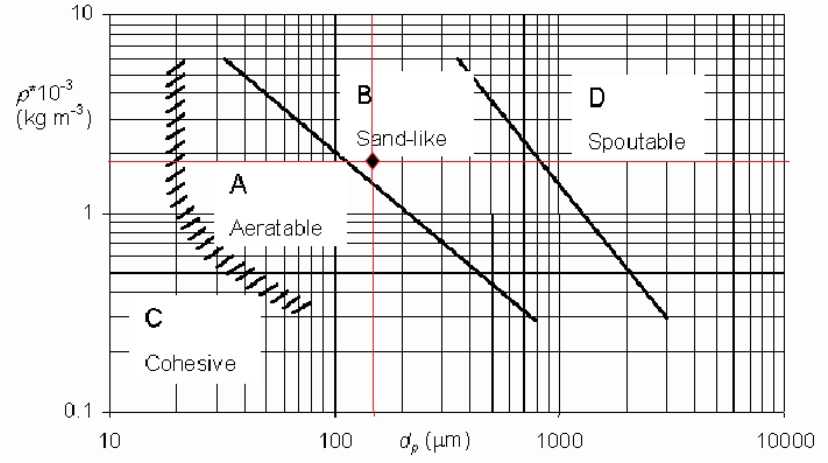

Figure 3.10: Powder classification chart after Geldart, where ρ^* is the density difference between the particles and the fluid [10].

3.7.1 Classification of the catalyst particles

The catalyst particles in the fluidized bed can be categorized in a group, as mentioned in Section 3.2.1. Figure 3.10 shows the diagram, that is used for the characterization. The density of the fluid is below 1 $\frac{\text{kg}}{\text{m}^3}$ and thus much smaller than the particle density of the catalyst. Therefore the fluid density is neglected. With a particle density of 1800 $\frac{\text{kg}}{\text{m}^3}$ and a particle diameter of 150 μm, the fluidized bed consists of Geldart B particles. Assumptions and calculations based on Geldart B particles are therefore legitimate.

3.7.2 Thermodynamic equilibrium models

Figure 3.11 shows, that both methods mentioned in Section 3.5.1 describe the thermodynamic behavior of the reaction system equally well. Molar fractions in this figure (except the one for water) are related to the dry gas mixture. This applies to all graphs and figures below. The slight deviations of the relaxation method at low temperatures are likely to disappear by setting a lower tolerance for the change in the number of moles Δn. The calculation time of the relaxation method depends on the tolerance for Δn but is always at least one order of magnitude higher than the time needed to solve the equilibrium formulations. Therefore, the latter method was preferred for future models.

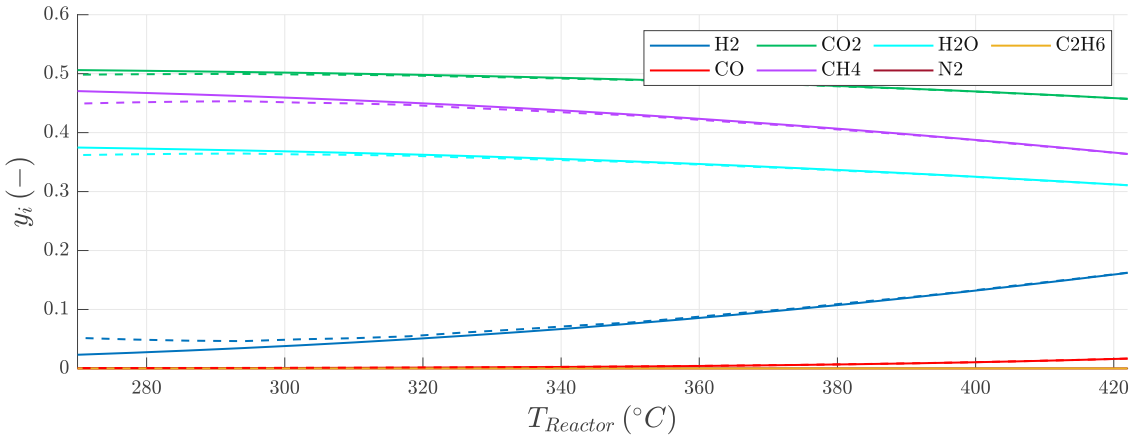

Figure 3.11: Comparison of the thermodynamic models. The continuous line shows the solution gained by solving the equilibrium formulations. The dashed line describes the solution of the relaxation method.

3.7.3 Selecting a rate equation

Table 3.4 shows different product gas compositions that were fed into the ICFB methanation reactor. For every gas mixture listed in Table 3.4, experimental data of the raw-SNG composition at different reactor temperatures are available. Gas mixture 1 was chosen as input for the fluidized bed model. Figure 3.12 shows the results obtained by using the four different rate equations described in Section 3.5.1. The rate equations proposed by Kopyscinski and Rönsch are not able to describe the experimental data. Kopyscinski's rate equation does not consider the reverse reaction of CO-methanation. Therefore, the conversion surpasses the equilibrium composition. Rönsch's approach seems to predict the CH_4-content quite well. However, it fails regarding the other components of the raw-SNG. That is probably caused by a too strong water-gas shift reaction in Rönsch's rate equation.

The rate equation proposed by Witte is too fast. The simulation results lie close to the thermodynamic equilibrium. On the other hand, the slope of the curve fits well with the data. For high temperatures, the raw-SNG composition trends towards equilibrium, whereas for low temperatures kinetics lower the conversion rate. As expected, the modified reaction rate (Witte*) reaches equilibrium composition perfectly, contrary to Witte's original approach, which deviates slightly from it.

Figure 3.13 shows the reaction course in the fluidized bed. It is the solution of the differential equations stated in Section 3.5.1, evaluated at every height increment. In Figure 3.13, the gas is divided into bubble and dense phase. The dense phase, where

Table 3.4: Composition and space velocity of selected product gases. Experimental data are available for all gas mixtures presented in the table.

Parameter	Unit	Gas mixtures						
		1	2	3	4	5	6	7
WHSV	$\frac{Nm^3}{h \cdot g_{cat}}$	1.5	1.5	1	0.8	1.5	1	1.5
H_2-content	mol. – %db	43.66	75	75	75	42.66	42.66	77.78
CO-content	mol. – %db	23.22	25	25	25	22.68	22.68	11.11
CO_2-content	mol. – %db	22.36	0	0	0	21.85	21.85	11.11
CH_4-content	mol. – %db	10.76	0	0	0	10.51	10.51	0
H_2O-content	mol. – %	20	0	0	0	20	20	0
N_2-content	mol. – %db	0	0	0	0	0	0	0
C_2H_4-content	mol. – %db	0	0	0	0	2.3	2.3	0

all the reactions take place, contains way less gas than the bubble phase. Therefore, the changes in the gas composition in the dense phase happen very fast in comparison to the bubble phase.

3.7.4 Estimation of rate equation parameters

To gain an accurate model, that describes the measured data well, a parameter estimation was carried out. The adjusted version of Witte's rate equation was used as the base function. Table 3.5 lists the estimated parameters and their respective initial values. The parameter estimation was done with data from gas mixture 1 (Table 3.4). Figure 3.14 shows the results gained by a simulation with the estimated parameters. As expected, the model performs well compared to the data it was trained with.

3.7.5 Model validation

To evaluate the performance of a model, validation is necessary. Cross-validation evaluates if the model reproduces suitable results compared to data that were not used for parameter estimation. Data gathered from experiments with gas mixtures 2-7 from Table 3.4 were used to validate the model. Gas mixtures 2-4 consist only of H_2 and CO

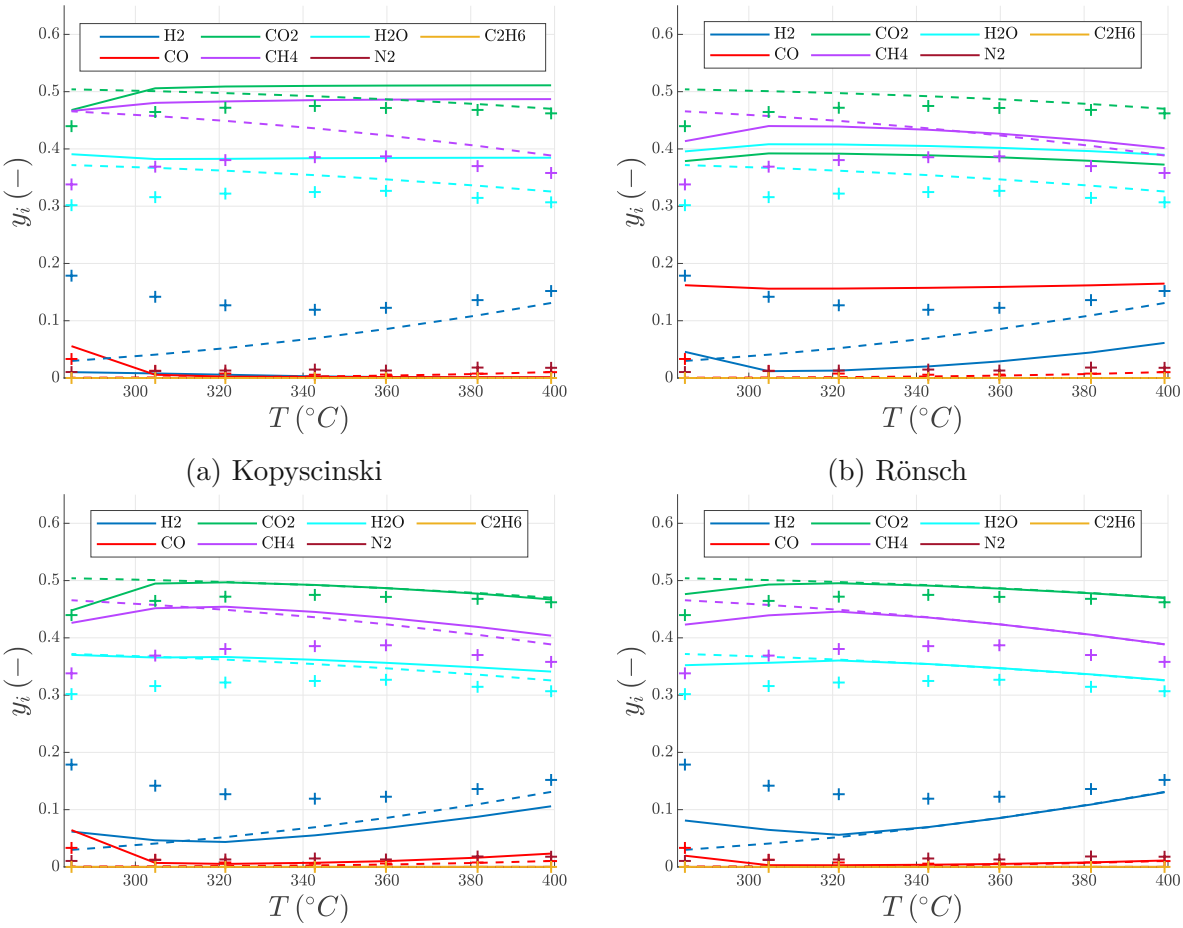

(a) Kopyscinski (b) Rönsch

(c) Witte (d) Witte*

Figure 3.12: Simulated raw-SNG composition for different kinetic approaches (a-d) in mole fractions. The simulation is given by the continuous line. Measured data are represented by crosses and the dashed line represents the thermodynamic limits.

Table 3.5: Initial values and results of the parameter estimation.

Parameters	Units	Initial value	Estimated value
$k_{0,\mathrm{WGS}}$	-	8.4	11.627
$k_{0,\mathrm{Meth}}$	-	1.08	0.1488
$E_{A,\mathrm{WGS}}$	$\frac{J}{mol}$	155.7	162.861
$E_{A,\mathrm{Meth}}$	$\frac{J}{mol}$	63.1	5.4061

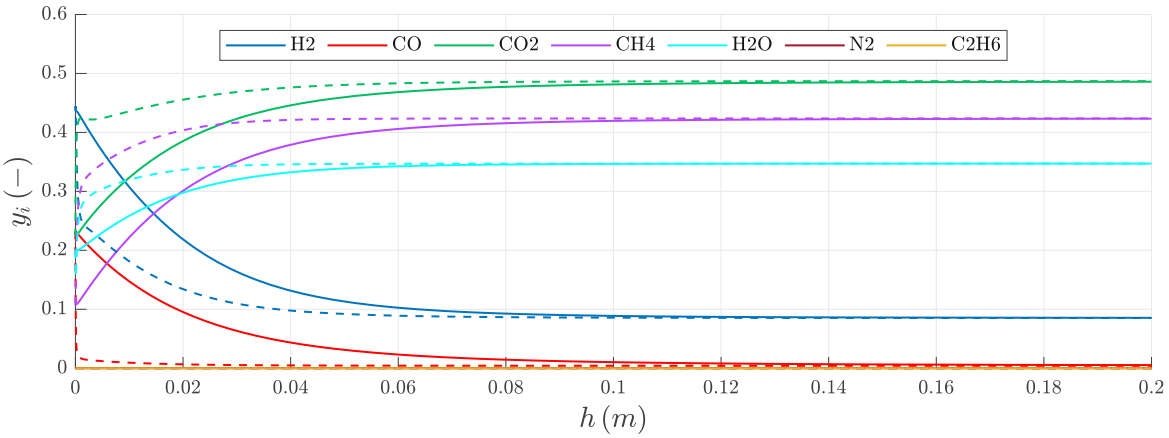

Figure 3.13: The graph shows the conversion of the product gas through the fluidized bed. The molar fractions of product gas are plotted over the height of the fluidized bed. The product gas is divided into bubble phase (continuous line) and dense phase (dashed line). As rate equation, the modified version of the one proposed by Witte was used.

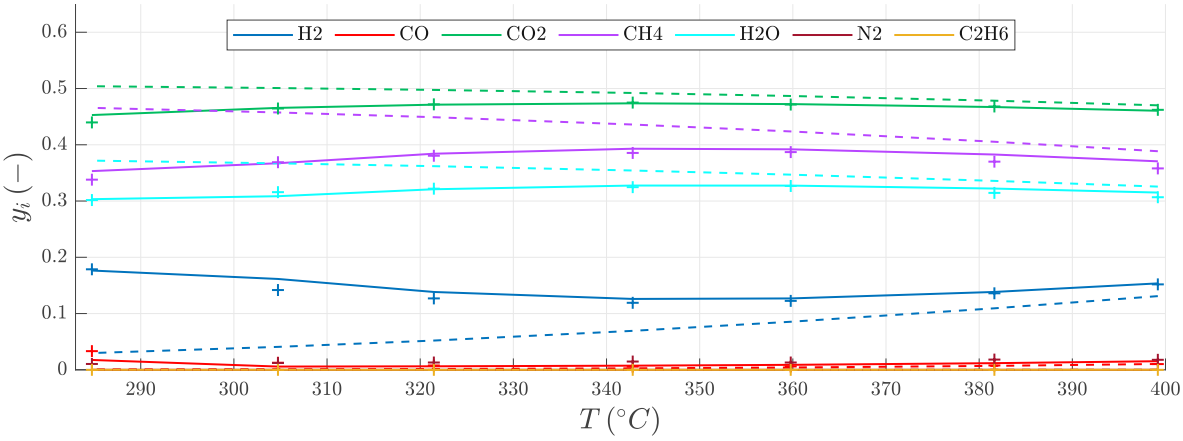

Figure 3.14: Comparison of measured data (crosses), chemical equilibrium (dashed line) and simulation results (continuous line). R^2= 0.9979.

in a stoichiometric mixture. Gas mixture 7 is a mixture of H_2 with small amounts of CO and CO_2. 5 and 6 are gas mixtures, which are intended to replicate real product gas. Figure 3.15 shows how the outputs generated by the model fit the respective data sets.
Overall, it can be said that the model shows a good performance. For the stoichiometric gas mixtures 2,3,4 and 7 the model shows minor deviations, especially in the lower temperature range. For the typical product gas compositions (Gas mixtures 1,5 and 6) the model fits well over the whole temperature range. There are dilutions of N_2 in the raw-SNG, due to the flushing of the pressure sensors.

3.7.6 Experimental results of the reactor cooling behavior

Figures B.1 and B.2 in Appendix B show the outcome of the three experiments described in Section 3.6.2. Figure B.2 includes experiments two and three in one figure. Each figure shows T_{Reactor} and the associated valve setting over time. As expected, T_{Reactor} rises if the valves are closed and falls when the valves get opened. At a constant valve setting, T_{Reactor} should reach a steady-state value after a certain time. Based on the data from experiment three, it can be seen that T_{Reactor} doesn't reach the same steady-state value after a relatively large change of the valve opening. Most likely, the time to reach the steady-state temperature was too short or other effects, which can't be measured, affected T_{Reactor}.

To compare the three experiments, it is necessary to convert the valve opening percentage into a volumetric flow rate $\dot{V}_{\text{air}}$. The conversion was performed with the help of characteristic curves for air pressures of 5 and 2.2 bar. The volumetric flow rates were measured with rotameters. Figure 3.16 shows the relation between $\dot{V}_{\text{air}}$ and the valve opening percentage. The two continuous lines are the approximations that give the characteristic curves. The curves are assumed to be linear in the region around the operating point.

3.7.7 Estimation of heat balance parameters

The parameter estimation was performed with chosen data from experiments one and three. The dataset covers two different cooling air pressures and minor changes in the product gas composition. Only data where the valve opening was close to the operating point was selected. Experiment two served as validation data set. Figure 3.17 shows the chosen data sets, the performed fit, and the corresponding cross-validation. As a quality criterion, the coefficient of determination R^2 from Section 3.5.2 was used again.

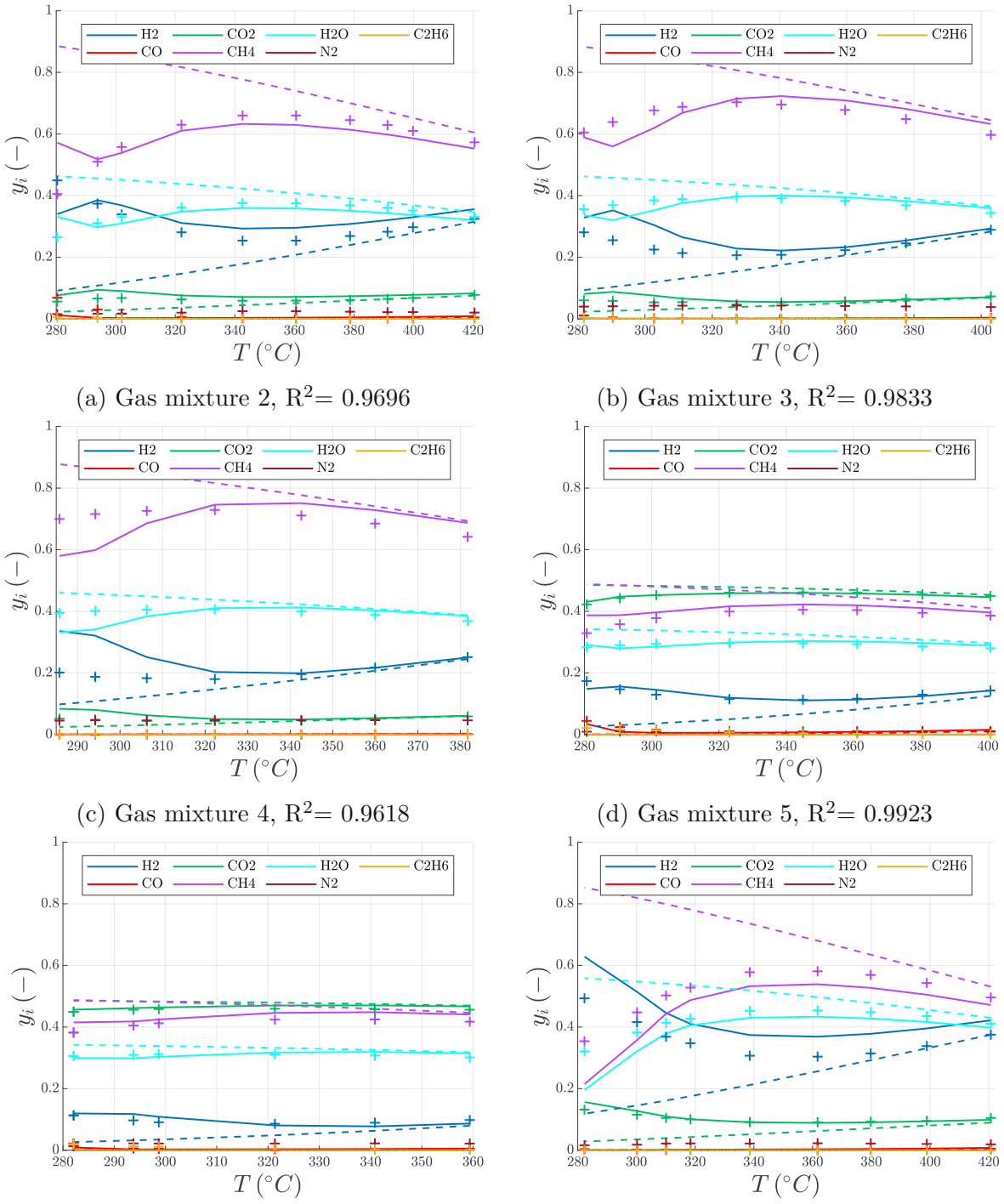

(a) Gas mixture 2, R^2= 0.9696

(b) Gas mixture 3, R^2= 0.9833

(c) Gas mixture 4, R^2= 0.9618

(d) Gas mixture 5, R^2= 0.9923

(e) Gas mixture 6, R^2= 0.9939

(f) Gas mixture 7, R^2= 0.9323

Figure 3.15: Cross-validation. Raw-SNG compositions calculated with the fluidized bed model (continuous line) are compared with data from experiments (crosses) and the thermodynamic equilibrium (dashed line). The gas mixtures used for the experiments are listed in Table 3.4.

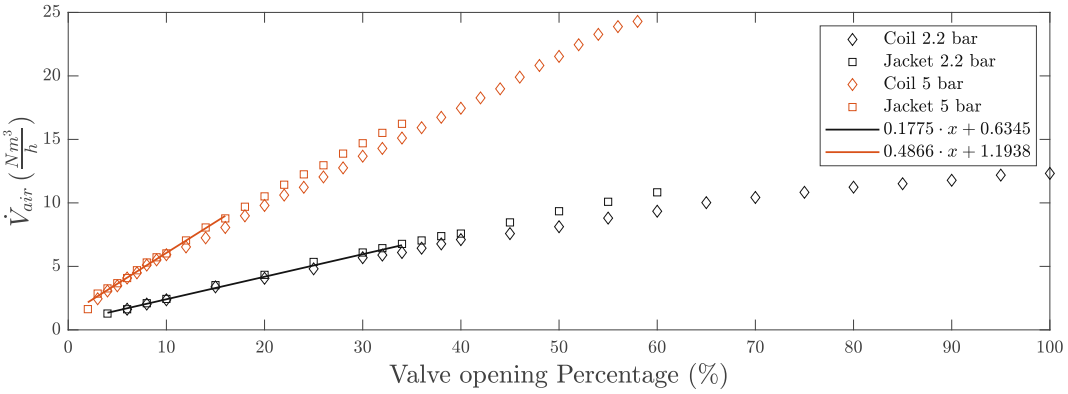

Figure 3.16: Volumetric flow rates at different valve opening percentages of the cooling air valves for 2.2 and 5 bar pressure. Additionally, two characteristic curves for volumetric flow rates around the operating points were approximated.

Table 3.6: Results of the parameter estimation.

Parameters	Estimated value
C_1	11.627
C_2	0.1488
C_3	162.861

Although the R^2 values of the fit and the cross-validation are satisfying, it can be seen from the figure, that the model doesn't reach the same steady-state temperatures as the real data. Due to the over-dimensioned air cooling system of the ICFB reactor, only a small area of the adjustment range of the cooling air valves could be used. That and the large time constants of the system are possible causes for the deviations in the thermal plant model. However, these errors are accepted in exchange for a simple model structure. The resulting model parameters are given by Table 3.6.

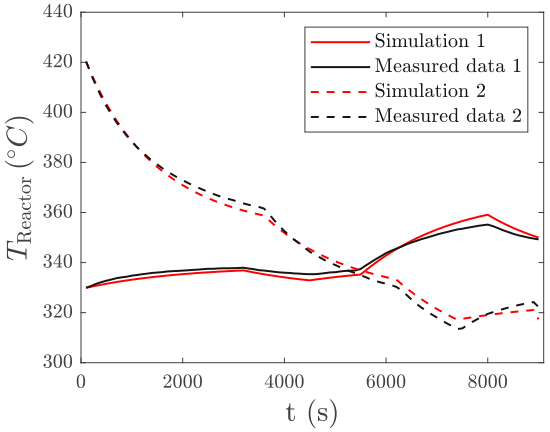

(a) Fit: $R^2 = 0.9898$

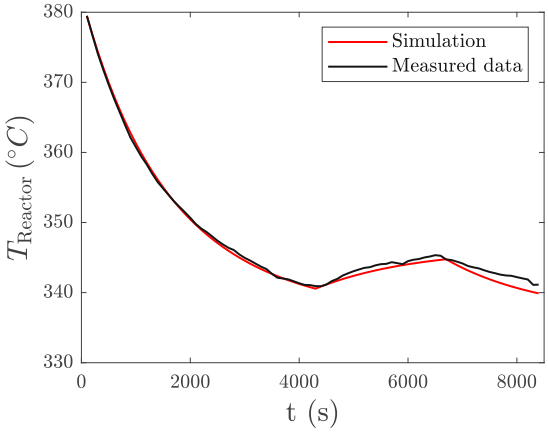

(b) Validation: $R^2 = 0.9951$

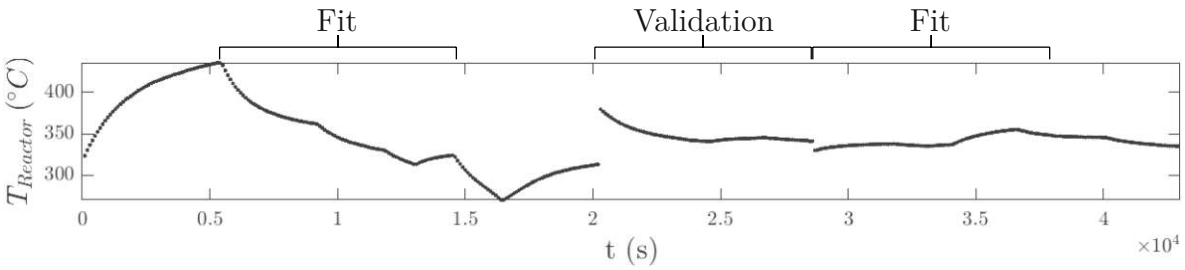

(c)

Figure 3.17: (a) Parameter fit, performed with data from experiments one and three. (b) Cross-validation with data from experiment two. (c) Illustration of the data that was taken for fitting and validation of the model parameters.

Chapter 4

Controller design

This chapter is about the design of the temperature controller. After a brief introduction to controller types, the calculation of the optimal setpoint is introduced. Then the chosen control structure and controller gains are presented. Lastly, this chapter includes also performance and robustness tests for the evaluation of the control design.

4.1 Controller types

In general, a distinction can be made between 2 different types of control: open-loop or feedforward control and closed-loop or feedback control.

4.1.1 Feedback control

Figure 4.1 shows the basic structure of a feedback controller, and the corresponding control quantities (w,e,u,z,y). The setpoint or reference variable w and the disturbance z are both inputs, while the y is the output variable. Feedback controllers measure the output y and compare it to w, which results in an error e. The goal of the controller is to minimize the error e. The controller changes the manipulated variable u, which influences the plant and leads ultimately to y approaching w.
Feedback controllers react to disturbances and to setpoint changes, by minimizing the resulting error. This characteristic makes feedback control stable against disturbances and changing parameters [70, 71].

4.1.2 Feedforward control

In feedforward control, there is no measurement of the output variable y. Feedforward control reacts only to incoming signals, which are the setpoint and in some cases measurable disturbances. In theory, feedforward controllers accommodate those dis-

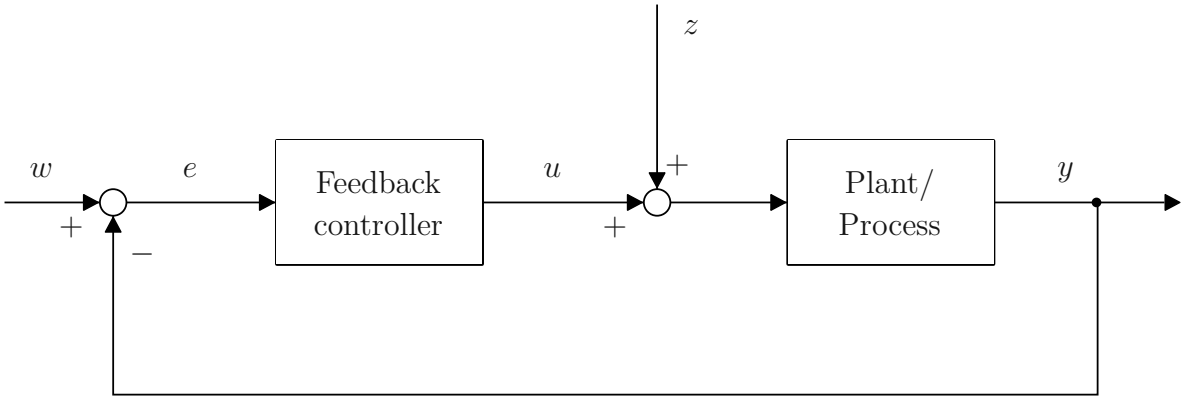

Figure 4.1: Schema of a basic feedback control structure.

turbances faster than feedback controller without a disturbance measurement, as they respond directly to the disturbance and not to the changing output variable. However, with no information on the output, feedforward control requires accurate knowledge of the manipulated variable and the disturbances and how they affect the output variable y. In addition, every single disturbance that acts on the system must be measurable and also taken into account to ensure good performance. Unknown disturbances or parameters that change over time can cause major problems in feedforward controlled systems. A way to eliminate these drawbacks is the combination of the feedforward controller with a feedback controller [70, 71].

4.2 Applied controller

In this work, a combined feedback-feedforward type controller is designed to control the reactor temperature T_{Reactor} for a maximal CH_4 yield. The idea is to react fast to measurable disturbances and set point changes with a static nonlinear feedforward controller while correcting model deviations and unmeasured disturbances with a PI controller. This is possible because the molar flows of all components in the product gas, that enters the reactor, can be measured online. Figure 4.2 shows a schema of such a controller. The control quantities are given by

$$
\begin{aligned}
w &= T_{\text{opt}} \\
y &= T_{\text{Reactor}} \\
u &= \text{Valve opening position} \\
\boldsymbol{z} &= [\dot{n}_{\text{H}_2,in}\ \dot{n}_{\text{CO},in}\ \dot{n}_{\text{CO}_2,in}\ \dot{n}_{\text{CH}_4,in}\ \dot{n}_{\text{H}_2\text{O},in}\ \dot{n}_{\text{N}_2,in}\ \dot{n}_{\text{C}_2\text{H}_4,in}]^{\boldsymbol{T}}
\end{aligned}
$$

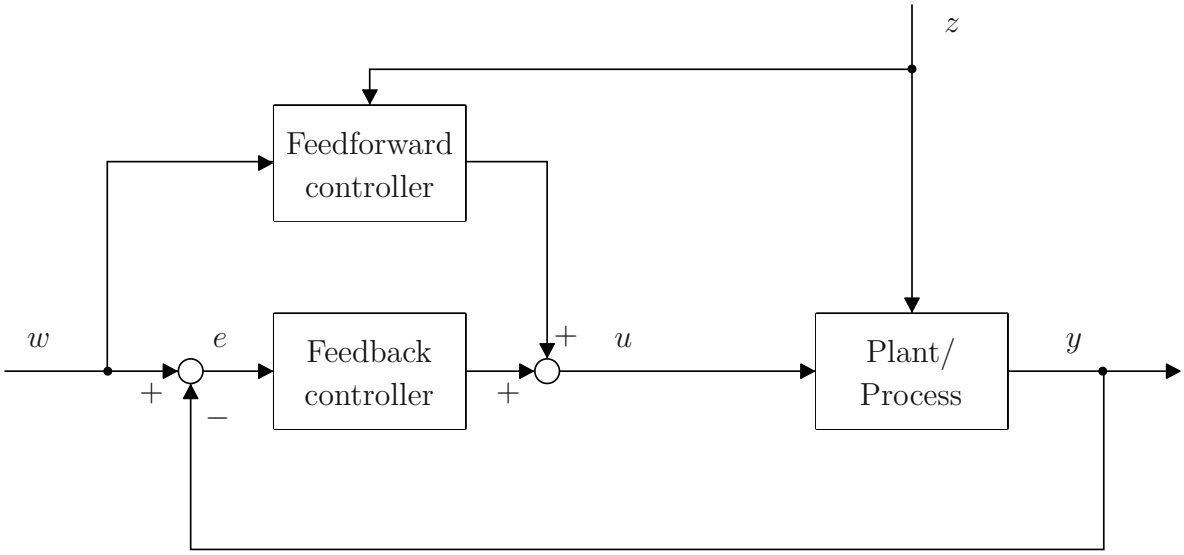

Figure 4.2: Schema of a controller with a feedback-feedforward type structure.

The optimal reactor temperature T_{opt} is calculated beforehand based on the molar flow rate of the product gas components. This control structure should accelerate the response of the system to measurable or predictable deviations while maintaining a robust control.

4.2.1 Setpoint calculation

The setpoint is defined by an algorithm, which calculates the reactor temperature that maximizes the CH_4 content in the raw-SNG. This temperature is defined as the optimal temperature T_{opt}. The algorithm evaluates the product gas at every time step, by calculating the resulting raw-SNG composition for reactor temperatures between 280 and 400 °C. The temperature interval is divided into 200 steps. The step number emerges as a trade-off between a high resolution and short calculation times. The reactor temperature, where the raw-SNG contains the most CH_4 is given out as T_{opt}.

4.2.2 Feedforward control design

Assuming that the model is accurate and there are no disturbances, the feedforward control should set the control valve position to reach the setpoint. When T_{Reactor} meets the setpoint, it shouldn't change further, reaching a steady state.

$$\left.\frac{dT_{\text{Reactor}}}{dt}\right|_{T_{\text{Reactor}}=T_{\text{opt}}} = 0 \tag{4.1}$$

Transforming (3.58) to $\dot{V}_{\text{air}}$ and considering the steady state, the transfer function of the static nonlinear feedforward controller is given by

$$\dot{V}_{\text{air}} = \frac{\dot{Q}_{\text{reaction}}(T_{\text{opt}}) - (T_{\text{opt}} - T_{\text{U}}) \cdot C_1}{(T_{\text{opt}} - T_{\text{U}}) \cdot C_2}. \tag{4.2}$$

4.2.3 Feedback control design

For feedback control, a conventional PI regulator is chosen. The transfer function G_{R} of the regulator is given by

$$G_{\text{R}}(s) = \frac{K_{\text{P}} \cdot s + K_{\text{I}}}{s}, \tag{4.3}$$

where K_{P} is the proportional gain and K_{I} is the integral gain. The output of a PI controller is composed of a part proportional to the error $e(t)$ and a part proportional to the integral of the error $\int e(t)\,dt$. The integral part of the regulator ensures a robust control behavior. The controller is designed via the pole placement method. It's a simple method, where the poles of the closed-loop system are chosen beforehand, and the gains K_{I} and K_{P} are then calculated accordingly.

Linearization

The pole placement method requires the transfer function of the closed loop system, which includes the transfer function of the plant. As the plant model is nonlinear, it has to be linearized around a steady-state operating point to get the transfer function. The nonlinear model is given as

$$\dot{T}_{\text{Reactor}} = f(T_{\text{Reactor}}, u, \boldsymbol{z}), \tag{4.4}$$

where u is the valve opening percentage and $\boldsymbol{z}$ are disturbances. Disturbances are all variables that can't be manipulated by the operator. However, some of the disturbances can be measured online, like the molar flow rates of the product gas components. In a steady-state operating point, where $\dot{T}_{\text{Reactor}} = 0$, applies

$$0 = f(T_{\text{Reactor},0}, u_0, \boldsymbol{z}_0). \tag{4.5}$$

The linearized plant model is then

$$\Delta\dot{T}_{\text{Reactor}} = A \cdot \Delta T_{\text{Reactor}} + b \cdot \Delta u \tag{4.6}$$

$$\Delta y = \Delta T_{\text{Reactor}}, \tag{4.7}$$

where $\Delta T_{\text{Reactor}} = T_{\text{Reactor}} - T_{\text{Reactor},0}$ and $\Delta u = u - u_0$. A and b are obtained by deriving the function partially to T_{Reactor} and u.

$$A = \frac{\partial f}{\partial T_{\text{Reactor}}} \qquad \text{and} \qquad b = \frac{\partial f}{\partial u}. \tag{4.8}$$

The derivatives are calculated numerically around the operating point. Let dT_{Reactor} and du be small steps in an order of magnitude of 10^{-6}, then

$$A = \frac{f((T_{\text{Reactor},0} + dT_{\text{Reactor}}), u_0, \boldsymbol{z}_0) - f(T_{\text{Reactor},0}, u_0, \boldsymbol{z}_0)}{dT_{\text{Reactor}}} \tag{4.9}$$

and

$$b = \frac{f(T_{\text{Reactor},0}, (u_0 + du), \boldsymbol{z}_0) - f(T_{\text{Reactor},0}, u_0, \boldsymbol{z}_0)}{du}. \tag{4.10}$$

Anti-wind-up

Considering the real application, the manipulated variable is limited to a range between 0 (fully closed valve) and 100 % (fully opened valve). For controllers with integral parts the so-called wind-up effect can occur, if the actuator limits are reached. The wind-up effect describes the case when the actuator is saturated, but the integrator part of the PI controller doesn't stop integrating the error. This leads to a high integrator output and further to long settling times [72].
An anti-wind-up is used to counteract the wind-up effect. In this work, a built-in Matlab function based on the back-calculating anti-wind-up method is used. It uses a feedback loop to discharge the integral part of the controller if actuator limits are reached [73].

4.3 Tests and Simulations

Different test runs are conducted to evaluate the performance and robustness of the final controller design. The system is fed with a predefined input, where the molar flows of the gas components are changing over time. The changes in the molar flows imply changes in the overall gas velocity in the reactor. Figure 4.3 shows the test track used in the simulation.

4.3.1 Performance test

To test if the performance of the feedback-feedforward controller is better than just a simple PI controller without the feedforward part, both variants are simulated. As

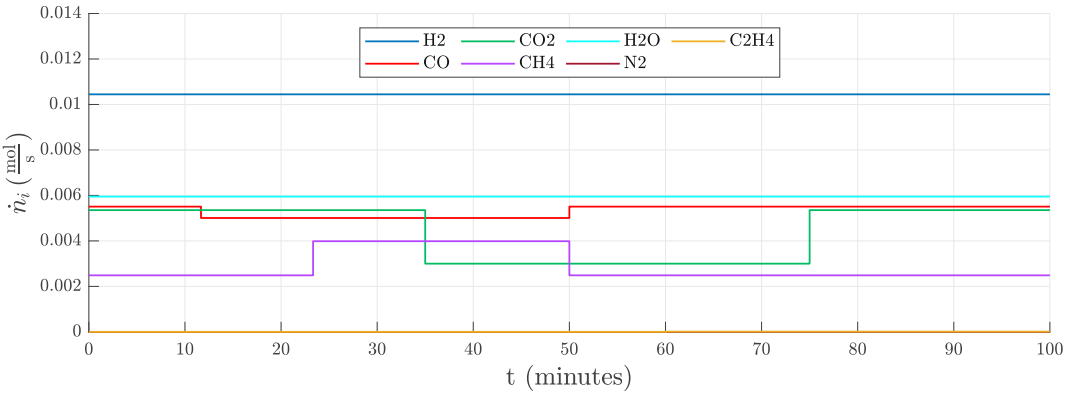

Figure 4.3: Input signal used in performance and robustness tests. The figure shows a typical product gas composition, that changes over time.

input for the simulation serves the test track from Figure 4.3. In addition, a simulation is performed in which the system is controlled only by the feedforward controller.

4.3.2 Robustness tests

Robustness tests are performed to check if the controller performs well regarding a wrong plant model. They help to evaluate the consequences of plant parameters that could change over time or deviations in the initial plant model.
In the robustness test, the plant model is modified intentionally, while the design and parameters of the controller stay the same. The plant model is changed so that the single terms in the heat balance deviate by 10%. This is done by multiplying the estimated parameters C_1, C_2 and C_3 from (3.58) by 1.1. Again, the test track from Section 4.3 serves as input for the simulation.
In a second test, white noise is filtered with a low pass filter and is added to the test track signals. By performing a simulation with noisy input signals, the robustness of the control structure against fast-changing disturbances can be evaluated. Figure 4.4 shows the noisy test track.

4.4 Results and discussion

This section contains the controller design with the pole placement method and the results of the performance and robustness tests.

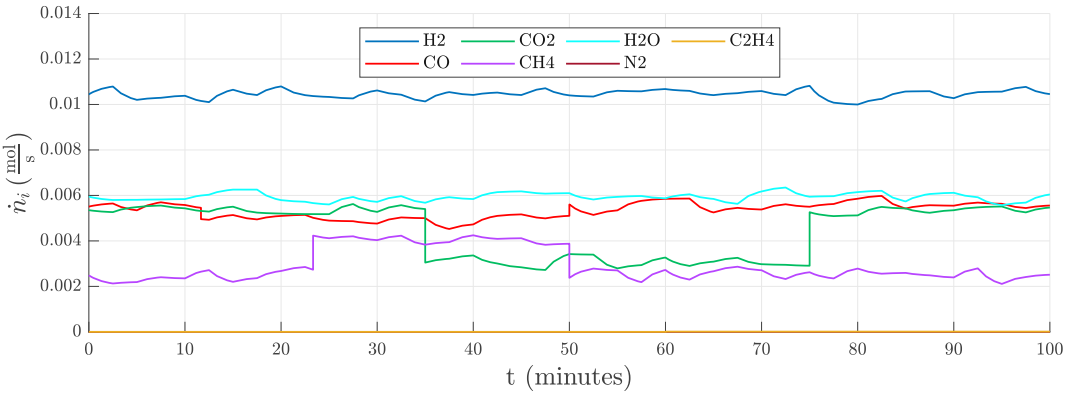

Figure 4.4: Input composition of the product gas from Figure 4.3 over time superimposed by noise.

4.4.1 Design of the PI controller

After linearizing the plant model, the transfer function of the plant G_{Plant} is given by

$$G_{\text{Plant}} = -\frac{0.005081}{s + 0.0006436}. \tag{4.11}$$

The open loop transfer function G_{OL} is calculated by multiplying G_{Plant} with (4.3).

$$G_{\text{OL}} = -\frac{0.005081 \cdot (K_{\text{P}} \cdot s + K_{\text{I}})}{s^2 + 0.0006436 \cdot s}. \tag{4.12}$$

The characteristic polynomial $P(s)$ of the closed loop system $P(s)$ is then

$$P(s) = s^2 + s \cdot (0.0006436 - 0.005081 \cdot K_{\text{P}}) - 0.005081 \cdot K_{\text{I}}. \tag{4.13}$$

For a relatively fast and stable PI controller, the two poles of the closed loop transfer function (s_1,s_2) are placed at $s_1 = -0.05$ and $s_2 = -0.01$. The gains of the controller are then matched so that $P(s)$ is consistent with the chosen poles. The gains resulted in

$$K_{\text{P}} = -11.6820 \qquad \text{and} \qquad K_{\text{I}} = -0.0984. \tag{4.14}$$

Figure 4.5 shows the step response of the designed PI controller, as well as the corresponding valve behavior. The reactor temperature meets the setpoint after approximately 50 seconds while ensuring that the valve opening does not reach the upper limit.

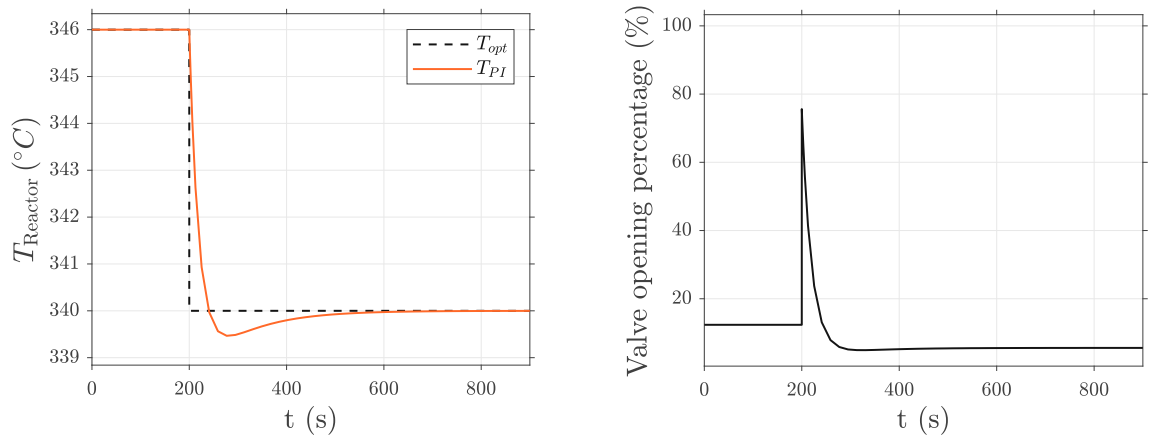

Figure 4.5: Step response of the designed PI controller. (a) Setpoint and output variable. (b) Manipulated variable.

4.4.2 Performance test

The performance test showed that the proposed controller performed better than the regular feedback control structures. The open loop control alone was too slow and couldn't follow the setpoint changes. The regular PI controller performed well and was as fast as the feedback-feedforward controller when facing a setpoint change. However, the feedback-feedforward controller performed better in situations where the setpoint was constant, but the disturbances changed. The ability to act instantly to measured product gas changes, instead of reacting to deviations of the output variable, is the advantage of the feedback-feedforward type control structure. Figure 4.6a shows the response of the different controllers to the input test track from Section 4.3. Figure 4.6b shows the corresponding behavior of the manipulated variable.

4.4.3 Robustness Test

The feedback-feedforward control structure performed well in the robustness tests. Different changes in the parameters of the heat balance made only small impacts on the controller performance. This shows that even if the model is possibly wrong, the controller still works. Figures 4.7 and 4.8 show the robustness tests of the controller. In Figure 4.7 all three parameters C_{1-3} were changed slightly (10%), while in Figure 4.8 the value of parameter C_2 was doubled to simulate a huge error in one parameter. In both cases, the PI controller manages to handle the model error. The impact of the PI control can be seen, when looking at the valve opening percentage in both figures. The feedforward part of the manipulated variable is way too high and gets adjusted by the

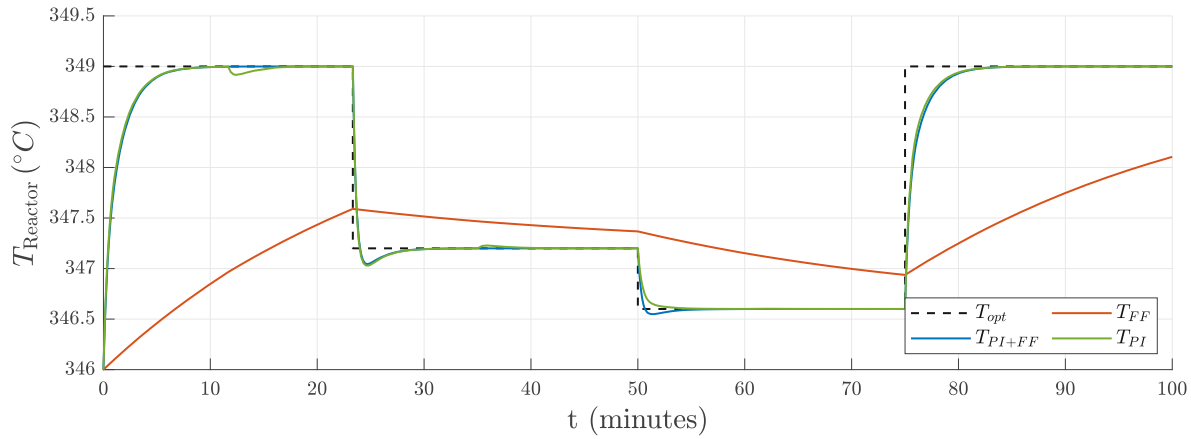

(a)

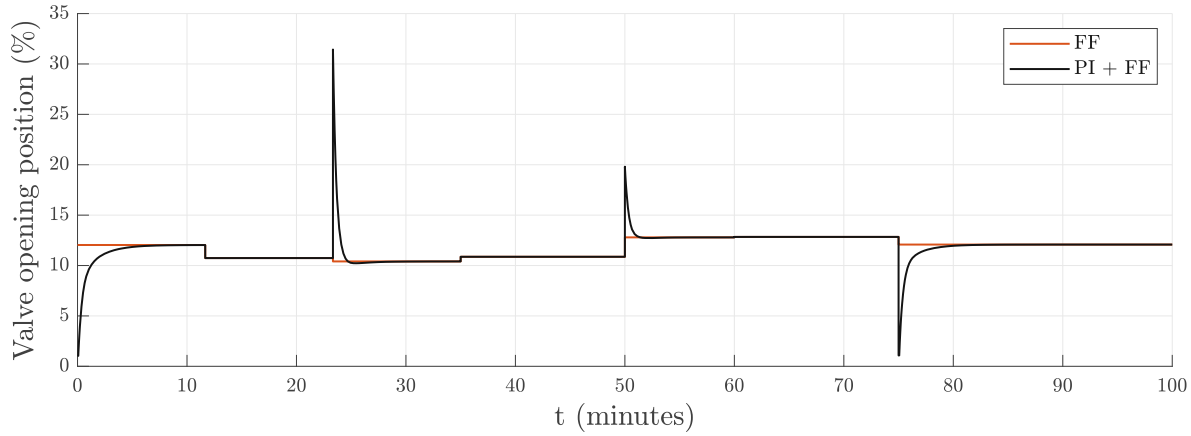

(b)

Figure 4.6: Performance test with different controller types. (a) Setpoint (T_{opt}) and output variable (green line = regular PI controller; blue line = feedback-feedforward controller; orange line = regular feedforward controller). (b) Manipulated variable (FF+PI) and feedforward part of the manipulated variable (FF).

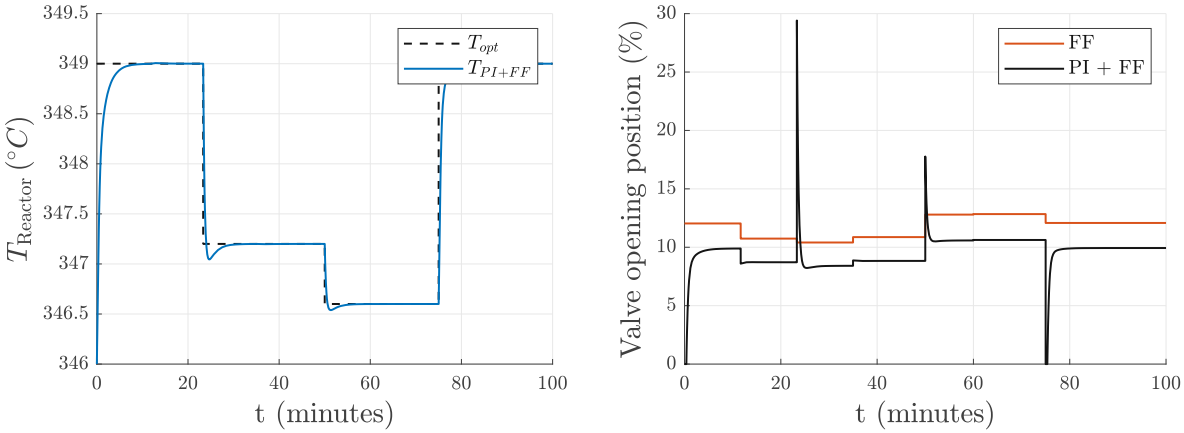

(a) (b)

Figure 4.7: Robustness test with 10% deviation in all parameters of the nonlinear plant model. (a) Setpoint (T_{opt}) and output variable. (b) Manipulated variable (FF+PI) and feedforward part of the manipulated variable (FF).

PI controller.

The last robustness check was made with noisy input signals. The corresponding test track is shown in Figure 4.4. Again, a model error was simulated by changing the parameters C_{1-3} by 10 %. Problems emerged with the calculation of the optimal setpoint. Due to the noise in the input, the setpoint fluctuated too much. Therefore the setpoint of this robustness test was set constant.
Figure 4.9 shows the results of the noisy input test. This test highlights the good interplay between feedforward and PI controller. The feedforward controller compensates for the fast changes of the noisy input, while the PI controller adjusts the offset that is caused by the error in the model.

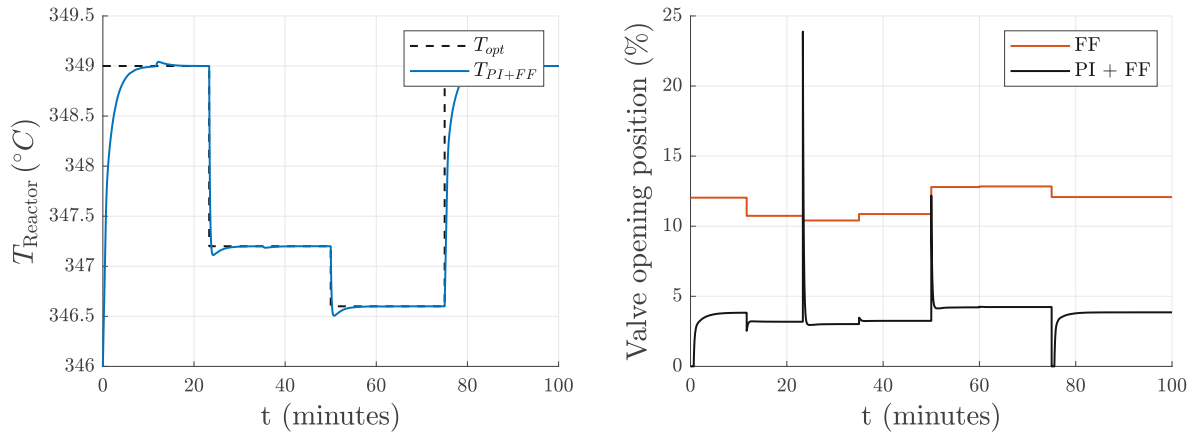

(a) (b)

Figure 4.8: Robustness test with 100% deviation in C_2 of the nonlinear plant model. (a) Setpoint (T_{opt}) and output variable. (b) Manipulated variable (FF+PI) and feedforward part of the manipulated variable (FF).

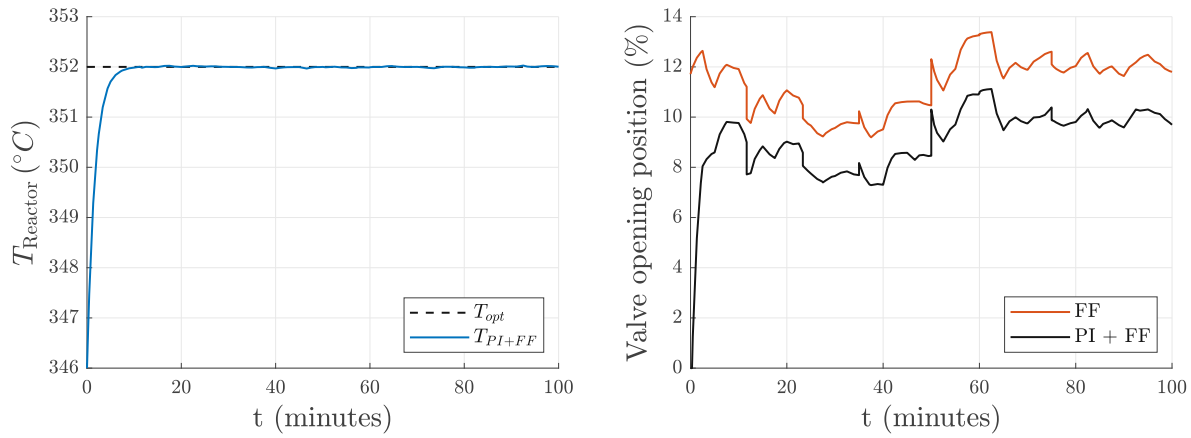

(a) (b)

Figure 4.9: Robustness test with noisy input signals and 10% deviation in all parameters of the nonlinear plant model. (a) Setpoint (T_{opt}) and output variable. (b) Manipulated variable (FF+PI) and feedforward part of the manipulated variable (FF).

Chapter 5

Conclusions

This work shows a method for the dynamic modeling of a fluidized bed methanation reactor and proposes a simple, yet effective feedback-feedforward type controller design. A satisfying model for the controller design could be obtained through the evaluation of experimental data. The model of the methanation reactor considers fluid dynamic, thermodynamic and kinetic aspects of fluidized bed methanation, but manages to waive elaborate kinetic studies of the catalyst.

The reactor model is able to predict the composition of the raw-SNG for the defined temperature range with satisfactory accuracy. It is likely that, with an adaptation of the parameters, the model can also be applied to other fluidized bed methanation reactors, since the kinetic plant model is mostly based on physical equations.

It was shown that the feedback-feedforward control structure could react faster to measurable disturbances in the product gas composition than a conventional feedback controller. This advantage should not be disregarded, especially for possible future applications, where online measurements of the product gas are available.

Through robustness tests, it was confirmed, that even a system with uncertainties in the thermal plant model can be controlled sufficiently well with the feedback-feedforward type controller. However, the thermal plant model should be refined for future applications, to further increase the positive impact of the feedforward part of the controller.

Summing up, it was possible to design a robust controller that has a high efficiency when an online measurement of the product gas composition and quantity is possible. The method that was used for the dynamic modeling of the plant can possibly be applied to model future plants, too. However, more attention should be paid to the thermal model, as it enhances the positive effects of the feedback-feedforward controller.

Future research in this area could look at replacing the static feedforward controller with a dynamic feedforward controller, to optimize the response to a rapidly changing setpoint. Also interesting would be the integration of the model and the controller in a control architecture that operates the whole SNG process chain. The combination of optimized sub-processes could lead to improvements in the SNG process.

Appendix A

Additional tables

Table A.1: Settings and operating conditions for experiment 1.

Experiment 1					
Parameter	Abbreviation	Unit		Dry gas	Wet gas
Cooling air pressure	P_{CA}	bar	5		
Molar fraction H_2	y_{H_2}	%		43.9	35.12
Molar fraction CO	y_{CO}	%		23.15	18.52
Molar fraction CO_2	y_{CO_2}	%		22.5	18
Molar fraction CH_4	y_{CH_4}	%		10.45	8.36
Molar fraction H_2O	y_{H_2O}	%			20
Pump settings annular region	$\dot{m}_{H_2O,ar}$	$\frac{kg}{h}$	0.3		
Pump settings draft tube	$\dot{m}_{H_2O,dt}$	$\frac{kg}{h}$	0.09		

Table A.2: Settings and operating conditions for experiment 2.

Experiment 2					
Parameter	Abbreviation	Unit		Dry gas	Wet gas
Cooling air pressure	P_{CA}	bar	2.2		
Molar fraction H_2	y_{H_2}	%		44.01	35.21
Molar fraction CO	y_{CO}	%		23.21	18.57
Molar fraction CO_2	y_{CO_2}	%		22.31	17.85
Molar fraction CH_4	y_{CH_4}	%		10.47	8.38
Molar fraction H_2O	y_{H_2O}	%			20
Pump settings annular region	$\dot{m}_{H_2O,ar}$	$\frac{kg}{h}$	0.3		
Pump settings draft tube	$\dot{m}_{H_2O,dt}$	$\frac{kg}{h}$	0.09		

Table A.3: Settings and operating conditions for experiment 3.

Experiment 3					
Parameter	Abbreviation	Unit		Dry gas	Wet gas
Cooling air pressure	P_{CA}	bar	2.2		
Molar fraction H_2	y_{H_2}	%		43.91	35.13
Molar fraction CO	y_{CO}	%		23.53	18.82
Molar fraction CO_2	y_{CO_2}	%		22.01	17.61
Molar fraction CH_4	y_{CH_4}	%		10.55	8.44
Molar fraction H_2O	y_{H_2O}	%			20
Pump settings annular region	$\dot{m}_{H_2O,ar}$	$\frac{kg}{h}$	0.3		
Pump settings draft tube	$\dot{m}_{H_2O,dt}$	$\frac{kg}{h}$	0.09		

Table A.4: Parameters for the calculation of rate and adsorption constants with their corresponding values

Parameter	Rönsch	Kopyscinski	Witte	Witte*
$k_{0,\mathrm{Meth,Klose}}$	$1.333 \cdot 10^{9}$ $\frac{\mathrm{mol}}{\mathrm{kg \cdot s}}$	-	-	-
$k_{0,\mathrm{Meth,Zhang}}$	$1.944 \cdot 10^{10}$ $\frac{\mathrm{mol}}{\mathrm{kg \cdot s}}$	-	-	-
$k_{0,\mathrm{Meth}}$	-	-	1.08	1.08
$k_{0,\mathrm{WGS}}$	$2.175 \cdot 10^{6}$ $\frac{\mathrm{mol}}{\mathrm{kg \cdot s \cdot bar}}$	-	8.4	8.4
$\ln(k_{0,\mathrm{Meth}}(T_{\mathrm{ref}}))$	-	0.08	-	-
$\ln(k_{0,\mathrm{WGS}}(T_{\mathrm{ref}}))$	-	2.12	-	-
$K_{0,\mathrm{C}}$	$5.8 \cdot 10^{-4}$ $\frac{1}{\mathrm{bar}^{0.5}}$	-	2.53 $\frac{1}{\mathrm{bar}^{1.5}}$	2.35 $\frac{1}{\mathrm{bar}^{1.5}}$
$K_{0,\mathrm{H}}$	$1.6 \cdot 10^{-2}$ $\frac{1}{\mathrm{bar}^{0.5}}$	-	-	-
$K_{0,\mathrm{CO}}$	$8.23 \cdot 10^{-5}$ $\frac{1}{\mathrm{bar}}$	-	-	-
$K_{0,\mathrm{H_2}}$	$6.12 \cdot 10^{-9}$ $\frac{1}{\mathrm{bar}}$	-	-	-
$K_{0,\mathrm{CH_4}}$	$6.65 \cdot 10^{-4}$ $\frac{1}{\mathrm{bar}}$	-	-	-
$K_{0,\mathrm{H_2O}}$	$1.77 \cdot 10^{5}$	-	-	-
$K_{0,\mathrm{OH}}$	-	-	0.67 $\frac{1}{\mathrm{bar}^{0.5}}$	0.67 $\frac{1}{\mathrm{bar}^{0.5}}$
$K_{0,\alpha}$	-	-	0.36 $\frac{1}{\mathrm{bar}^{2}}$	-
$\ln(K_{0,\mathrm{OH}}(T_{\mathrm{ref}}))$	-	-0.40	-	-
$\ln(K_{0,\mathrm{CH}}(T_{\mathrm{ref}}))$	-	0.93	-	-
$\ln(K_{0,\alpha}(T_{\mathrm{ref}}))$	-	-1.02	-	-
$E_{\mathrm{A,Meth}}$	103000 $\frac{\mathrm{J}}{\mathrm{mol}}$	-	63100 $\frac{\mathrm{J}}{\mathrm{mol}}$	63100 $\frac{\mathrm{J}}{\mathrm{mol}}$
$E_{\mathrm{A,WGS}}$	62000 $\frac{\mathrm{J}}{\mathrm{mol}}$	-	155700 $\frac{\mathrm{J}}{\mathrm{mol}}$	155700 $\frac{\mathrm{J}}{\mathrm{mol}}$
$\frac{E_{\mathrm{A,Meth}}}{R \cdot T_{\mathrm{ref}}}$	-	12.7	-	-
$\frac{E_{\mathrm{A,WGS}}}{R \cdot T_{\mathrm{ref}}}$	-	31.3	-	-
ΔH_{C}	-42000 $\frac{\mathrm{J}}{\mathrm{mol}}$	-	-50700 $\frac{\mathrm{J}}{\mathrm{mol}}$	-50700 $\frac{\mathrm{J}}{\mathrm{mol}}$
ΔH_{H}	-16000 $\frac{\mathrm{J}}{\mathrm{mol}}$	-	-	-
ΔH_{CO}	-70650 $\frac{\mathrm{J}}{\mathrm{mol}}$	-	-	-
$\Delta H_{\mathrm{H_2}}$	-82900 $\frac{\mathrm{J}}{\mathrm{mol}}$	-	-	-
$\Delta H_{\mathrm{CH_4}}$	-38280 $\frac{\mathrm{J}}{\mathrm{mol}}$	-	-	-
$\Delta H_{\mathrm{H_2O}}$	88680 $\frac{\mathrm{J}}{\mathrm{mol}}$	-	-	-
ΔH_{OH}	-	-	-87500 $\frac{\mathrm{J}}{\mathrm{mol}}$	-87500 $\frac{\mathrm{J}}{\mathrm{mol}}$
ΔH_{α}	-	-	-1700 $\frac{\mathrm{J}}{\mathrm{mol}}$	-
$\frac{\Delta H_{\mathrm{OH}}}{R \cdot T_{\mathrm{ref}}}$	-	-17.6	-	-
$\frac{\Delta H_{\mathrm{CH}}}{R \cdot T_{\mathrm{ref}}}$	-	-10.2	-	-
$\frac{\Delta H_{\alpha}}{R \cdot T_{\mathrm{ref}}}$	-	-1.02	-	-

Appendix B

Additional Figures

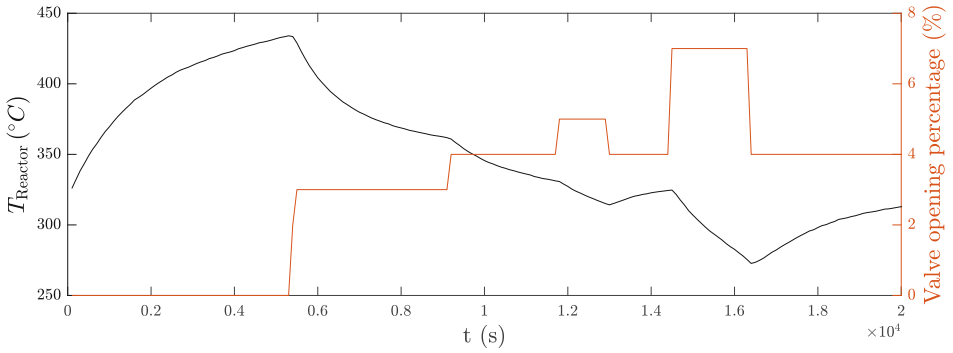

Figure B.1: Data of experiment one. The black line shows the reactor temperature over time and the orange line shows the corresponding valve setting.

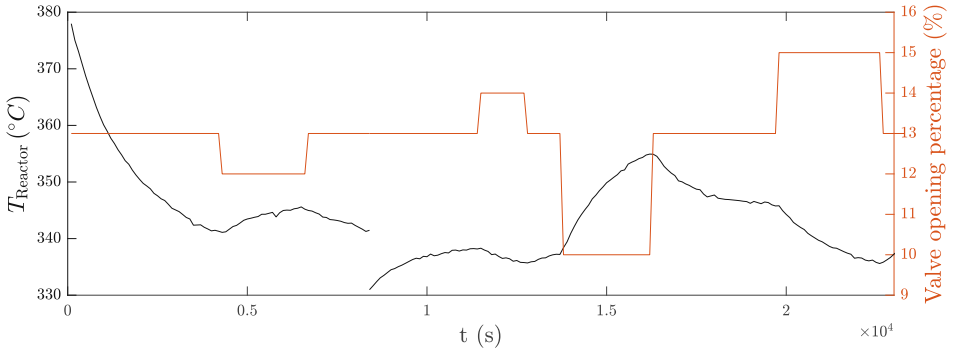

Figure B.2: Data of experiments two and three. The black line shows the reactor temperature over time and the orange line shows the corresponding valve setting.

List of Tables

List of Figures

Bibliography

[1] IEA. Final consumption by sector and source, OECD(https://www.iea.org/data-and-statistics/charts/final-consumption-by-sector-and-source-oecd-2018), 2018.

[2] M. Kaltschmitt, H. Hartmann, and H. Hofbauer. *Energie aus Biomasse : Grundlagen, Techniken und Verfahren.* Springer Berlin Heidelberg Imprint: Springer Vieweg, Berlin, Heidelberg, 3 edition, 2016.

[3] J. C.Schmid, F. Benedikt, J. Fuchs, A. M. Mauerhofer, S. Müller, and H. Hofbauer. Syngas for biorefineries from thermochemical gasification of lignocellulosic fuels and residues—5 years' experience with an advanced dual fluidized bed gasifier design. *Biomass Conversion and Biorefinery*, 11, 2021.

[4] S. Rönsch, J. Schneider, S. Matthischke, M. Schlüter, M. Götz, J. Lefebvre, P. Prabhakaran, and S. Bajohr. Review on methanation - from fundamentals to current projects. *Fuel*, 166:276–296, 2016.

[5] J. Lefebvre, M. Götz, S. Bajohr, R. Reimert, and T. Kolb. Improvement of three-phase methanation reactor performance for steady-state and transient operation. *Fuel processing technology*, 132:83–90, 2015.

[6] A. Bartik, B. Haddadi, C. Jordan, C. Slouka, E. Wartha, F. Benedikt, M. Bösenhofer, R. Martzy, W. Wukovits, J. Fuchs, S. Müller, and H. Hofbauer. Development of an internally circulating fluidized bed for catalytic methanation of syngas development of an internally circulating fluidized bed for catalytic methanation of syngas. *16th Minisymposium Verfahrenstechnik and 7th Partikelforum*, 2020.

[7] H. Hofbauer. *Unterlagen zur Vorlesung Wirbelschichttechnik.* TU Wien, 2020.

[8] J. R. Grace. Contacting modes and behaviour classification of gas—solid and other two-phase suspensions. *The Canadian Journal of Chemical Engineering*, 64(3):353–363, 1986.

[9] J. Kopyscinski. *Production of synthetic natural gas in a fluidized bed reactor.* ETH/PSI, 2010.

[10] T. M. Rosa. Synthesis of amine-modified aerogel sorbents and metal-organic framework-5 (MOF-5) membranes for carbon dioxide separation. Technical report, Arizona State University, 2010.

[11] Österreichischer Verein für Gas und Wasserkraft. Gasbeschaffenheit, 2021.

[12] J. Kopyscinski, T. J. Schildhauer, and S. M.A. Biollaz. Production of synthetic natural gas (SNG) from coal and dry biomass - a technology review from 1950 to 2009. *Fuel*, 89:1763–1783, 2010.

[13] H. Hiller, R. Reimert, F. Marschner, H. Renner, W. Boll, E. Supp, M. Brejc, W. Liebner, G. Schaub, G. Hochgesand, et al. Gas production ullmann's encyclopedia of industrial chemistry. 2006.

[14] S. Fendt, M. Gaderer, and H. Spliethoff. Synthetic natural gas (SNG) - state-of-the-art technology and application review. *19th European Biomass Coference and Exhibition*, 2011.

[15] S. Luo, B. Xiao, X. Guo, Z. Hu, S. Liu, and M. He. Hydrogen-rich gas from catalytic steam gasification of biomass in a fixed bed reactor: Influence of particle size on gasification performance. *International Journal of Hydrogen Energy*, 34:1260–1264, 2009.

[16] A. A. Ahmad, N. A. Zawawi, F. H. Kasim, A. Inayat, and A. Khasri. Assessing the gasification performance of biomass: A review on biomass gasification process conditions, optimization and economic evaluation. *Renewable and Sustainable Energy Reviews*, 53:1333–1347, 2016.

[17] F. Benedikt, J. Fuchs, J. C. Schmid, S. Müller, and H. Hofbauer. Advanced dual fluidized bed steam gasification of wood and lignite with calcite as bed material. *Korean Journal of Chemical Engineering*, 34:2548–2558, 2017.

[18] W. Zhang, H. Liu, I. Ul Hai, Y. Neubauer, P. Schröder, H. Oldenburg, A. Seilkopf, and A. Kolling. Gas cleaning strategies for biomass gasification product gas. *International Journal of Low-Carbon Technologies*, 7:69–74, 2012.

[19] M. Asadullah. Biomass gasification gas cleaning for downstream applications: A comparative critical review. *Renewable and Sustainable Energy Reviews*, 40:118–132, 2014.

[20] J. Kopyscinski, T. J. Schildhauer, F. Vogel, S. M.A. Biollaz, and A. Wokaun. Applying spatially resolved concentration and temperature measurements in a catalytic plate reactor for the kinetic study of CO methanation. *Journal of Catalysis*, 271:262–279, 2010.

[21] P. Sabatier and J. B. Senderens. Comptes rendus des séances de l'académie des sciences, section vi–chimie. *Paris: Imprimerie Gauthier-Villars*, 1902.

[22] M. Seemann and H. Thunman. *Methane synthesis*. Elsevier, 2019.

[23] C. Rhodes, G. J. Hutchings, and A. M. Ward. Water-gas shift reaction: finding the mechanistic boundary. *Catalysis Today*, 23:43–58, 1995.

[24] A. Bartik, F. Benedikt, A. Lunzer, C. Walcher, S. Müller, and H. Hofbauer. Thermodynamic investigation of SNG production based on dual fluidized bed gasification of biogenic residues. *Biomass Conversion and Biorefinery*, 11(1):95–110, 2021.

[25] M. A. Vannice. The catalytic synthesis of hydrocarbons from HJCO mixtures over the group VIII metals i. the specific activities and product distributions of supported metals. *Journal of catalysis*, 31:449–461, 1975.

[26] J. Gao, Q. Liu, F. Gu, B. Liu, Z. Zhong, and F. Su. Recent advances in methanation catalysts for the production of synthetic natural gas. *RSC Advances*, 5:22759–22776, 2015.

[27] L. Kiewidt and J. Thöming. Predicting optimal temperature profiles in single-stage fixed-bed reactors for CO2-methanation. *Chemical Engineering Science*, 132:59–71, 2015.

[28] H. Huang, H. Xiao, and S. Yang. Carbon flow and energy flow analyses of a lurgi coal-to-sng process. *Applied Thermal Engineering*, 125:891–903, 2017.

[29] J. H. Jensen, J. M. Poulsen, and N. U. Andersen. From coal to clean energy. *Nitrogen+ syngas*, 310:34–38, 2011.

[30] H. Harms, B. Höhlein, and A. Skov. Methanisierung kohlenmonoxidreicher Gase beim Energie-Transport. *Chemie Ingenieur Technik*, 52(6):504–515, 1980.

[31] W. J. Lee, C. Li, H. Prajitno, J. Yoo, J. Patel, Y. Yang, and S. Lim. Recent trend in thermal catalytic low temperature CO2 methanation: A critical review. *Catalysis Today*, 368:2–19, 2021.

[32] S. Matthischke, S. Roensch, and R. Güttel. Start-up time and load range for the methanation of carbon dioxide in a fixed-bed recycle reactor. *Industrial and Engineering Chemistry Research*, 57:6391–6400, 2018.

[33] T. J. Schildhauer and S. M. A. Biollaz. Reactors for catalytic methanation in the conversion of biomass to synthetic natural gas (SNG). *Chimia*, 69:603–607, 2015.

[34] H. L. Huynh and Z. Yu. CO2 methanation on hydrotalcite-derived catalysts and structured reactors: A review. *Energy Technology*, 8, 2020.

[35] M. Götz, F. Ortloff, R. Reimert, O. Basha, B. I. Morsi, and T. Kolb. Evaluation of organic and ionic liquids for three-phase methanation and biogas purification processes. *Energy and Fuels*, 27:4705–4716, 2013.

[36] J. R. Grace, I. A. Abba, H. Bi, and M. L. Thompson. Fluidized bed catalytic reactor modeling across the flow regimes. *The Canadian Journal of Chemical Engineering*, 77(2):305–311, 1999.

[37] B. Liu and S. Ji. Comparative study of fluidized-bed and fixed-bed reactor for syngas methanation over Ni-W/TiO2-SiO2 catalyst. *Journal of Energy Chemistry*, 22:740–746, 2013.

[38] A. Tremel, M. Gaderer, and H. Spliethoff. Small-scale production of synthetic natural gas by allothermal biomass gasification. *International Journal of Energy Research*, 37:1318–1330, 2013.

[39] ON. Önorm en 16726:2019 10 01, 2019.

[40] ON. Önorm en 16723-1:2017 01 01, 2017.

[41] T. J. Schildhauer and S. M. Biollaz. *Synthetic natural gas from coal, dry biomass, and power-to-gas applications*. Wiley, 2016.

[42] J. G. Yates and P. Lettieri. *Fluidized-bed reactors: processes and operating conditions*. Particle technology series. Springer International Publishing, 2016.

[43] D. Geldart. Types of gas fluidization. *Powder technology*, 7(5):285–292, 1973.

[44] A. Farshi, F. Naderi, and J. Sadeghzadeh. Approch to modelling of gas-solid fluidized bed reactor. *Petroleum and Coal*, 48(2):53–62, 2006.

[45] D. Kunii and O. Levenspiel. Bubbling fluidized-bed model. *Industrial & engineering chemistry fundamentals*, 7(3):446, 1968.

[46] K. Kato and C. Y. Wen. Bubble assemblage model for fluidized bed catalytic reactors. *Chemical engineering science*, 24(8):1351–1369, 1969.

[47] H. D. Baehr. *Thermodynamik : Grundlagen und technische Anwendungen. Mit zahlreichen Tabellen sowie 74 Beispielen.* Springer-Lehrbuch. Springer, 12 edition, 2005.

[48] J. Gao, Y. Wang, Y. Ping, G. Hu, D.and Xu, F. Gu, and F. Su. A thermodynamic analysis of methanation reactions of carbon oxides for the production of synthetic natural gas. *RSC advances*, 2(6):2358–2368, 2012.

[49] A. Beuls, C. Swalus, M. Jacquemin, G. Heyen, A. Karelovic, and P. Ruiz. Methanation of CO2: further insight into the mechanism over Rh/γ-Al2O3 catalyst. *Applied Catalysis B: Environmental*, 113:2–10, 2012.

[50] M. Greyson. *Synthesis of methane*, volume 5137. US Department of the Interior, Bureau of Mines, 1955.

[51] M. D. Lechner. *Einführung in die Kinetik: Chemische Reaktionskinetik und Transporteigenschaften.* Springer Berlin Heidelberg, Berlin, Heidelberg, 2018.

[52] C. H. Hamann, D. Hoogestraat, and R. Koch. *Grundlagen der Kinetik : Von Transportprozessen zur Reaktionskinetik.* Springer Berlin Heidelberg Imprint: Springer Spektrum, Berlin, Heidelberg, 2017.

[53] J. T. Cobb and R. C. Streeter. Evaluation of fluidized-bed methanation catalysts and reactor modeling. *Industrial and Engineering Chemistry Process Design and Development*, 18:672–679, 1979.

[54] The Langmuir isotherm (https://chem.libretexts.org/bookshelves/physical_and_theoretical_chemistry_textbook_maps/book%3a_surface_science_(nix)/03%3a_the_langmuir_isotherm), 2022.

[55] J. Witte, J. Settino, S. M.A. Biollaz, and T. J. Schildhauer. Direct catalytic methanation of biogas – part i: New insights into biomethane production using rate-based modelling and detailed process analysis. *Energy Conversion and Management*, 171:750–768, 2018.

[56] S. Rönsch, J. Köchermann, J. Schneider, and S. Matthischke. Global reaction kinetics of CO and CO2 methanation for dynamic process modeling. *Chemical Engineering & Technology*, 39(2):208–218, 2016.

[57] J. Zhang, N. Fatah, S. Capela, Y. Kara, O. Guerrini, and A. Y. Khodakov. Kinetic investigation of carbon monoxide hydrogenation under realistic conditions of methanation of biomass derived syngas. *Fuel*, 111:845–854, 2013.

[58] J. Klose and M. Baerns. Kinetics of the methanation of carbon monoxide on an alumina-supported nickel catalyst. *Journal of Catalysis*, 85(1):105–116, 1984.

[59] P. Stephan, S. Kabelac, M. Kind, D. Mewes, K. Schaber, and T. Wetzel. *VDI-Wärmeatlas: Fachlicher Träger VDI-Gesellschaft Verfahrenstechnik und Chemieingenieurwesen*. Springer Reference Technik. Springer Berlin / Heidelberg, Berlin, Heidelberg, 12 edition, 2019.

[60] C. R. Wilke. A viscosity equation for gas mixtures. *The journal of chemical physics*, 18(4):517–519, 1950.

[61] J. Werther. Die Bedeutung der Blasenkoaleszenz für die Auslegung von Gas/Feststoff-Wirbelschichten. *Chemie Ingenieur Technik*, 48(4):339–339, 1976.

[62] S. P. Sit and J. R. Grace. Effect of bubble interaction on interphase mass transfer in gas fluidized beds. *Chemical Engineering Science*, 36(2):327–335, 1981.

[63] C. R. Wilke and C. Y. Lee. Estimation of diffusion coefficients for gases and vapors. *Industrial & Engineering Chemistry*, 47(6):1253–1257, 1955.

[64] E. N. Fuller, K. Ensley, and J. C. Giddings. Diffusion of halogenated hydrocarbons in helium. the effect of structure on collision cross sections. *The Journal of Physical Chemistry*, 73(11):3679–3685, 1969.

[65] E. N. Fuller, P. D. Schettler, and J. C. Giddings. New method for prediction of binary gas-phase diffusion coefficients. *Industrial & Engineering Chemistry*, 58(5):18–27, 1966.

[66] B. J. McBride. *Coefficients for calculating thermodynamic and transport properties of individual species*, volume 4513. National Aeronautics and Space Administration, 1993.

[67] Pröll T. *Applied modelling in process engineering and energy technology*. TU Wien, 2016.

[68] Inc. The MathWorks. Optimization toolbox (https://de.mathworks.com/products/optimization.html), 2022.

[69] M. Baerns, A. Behr, A. Brehm, J. Gmehling, H. Hofmann, and U. Onken. *Technische Chemie*. John Wiley & Sons, 2013.

[70] L. Keviczky, R. Bars, J. Hetthéssy, and C. Bányász. *Control engineering*. Springer, 2019.

[71] C. P. Underwood. *HVAC control systems: Modelling, analysis and design*. Routledge, 2002.

[72] C. Bohn and D.P. Atherton. An analysis package comparing PID anti-windup strategies. *IEEE Control Systems Magazine*, 15(2):34–40, 1995.

[73] Inc. The MathWorks. Anti-windup control using a pid controller (https://de.mathworks.com/help/simulink/slref/anti-windup-control-using-a-pid-controller.html), 2022.